

Computational Study of Impact and Spreading of a Compound Droplet on a Flat Surface as
a Model for Single Cell Epitaxy

by

Gözde Kaynak

A Thesis Submitted to the
Graduate School of Engineering
in Partial Fulfillment of the Requirements for
the Degree of

Master of Science
in
Mechanical Engineering

Koc University

July 2010

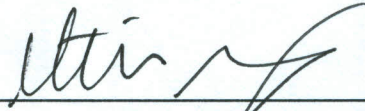
Koc University
Graduate School of Sciences and Engineering

This is to certify that I have examined this copy of a master's thesis by

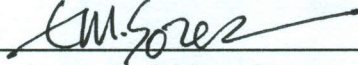
Gözde Kaynak

and have found that it is complete and satisfactory in all respects,
and that any and all revisions required by the final
examining committee have been made.

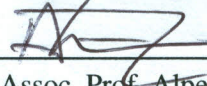
Committee Members:



Assoc. Prof. Metin Muradoğlu (Advisor)



Assoc. Prof. Murat Sözer



Assoc. Prof. Alper Kiraz

Date:

8/07/2010

To my family

ABSTRACT

Impact and spreading of a compound viscous droplet on a substrate are studied computationally using front-tracking method as a model for single cell epitaxy, a technology developed to create 2D and 3D tissues cell by cell by printing cell-encapsulating droplets on a substrate using ink-jet printing method. The success of cell printing depends on cell viability during the printing process. In the present model, the cell is modeled as a highly viscous Newtonian droplet encapsulated by a less viscous liquid. Simulations are performed for a range of dimensionless parameters to probe deformation and rate of deformation of the cell, which are hypothesized to be the major cause of cell damage. It is found that deformation of inner droplet increases: as Reynolds number increases; as the diameter ratio of encapsulating droplet to cell decreases; as the ratio of surface tensions of air-solution interface to solution-cell interface increases; as the viscosity ratio of cell to encapsulating droplet decreases; or as the equilibrium contact angle decreases. It is observed that maximum deformation has local minimum at Weber number $We = 2$. Thereafter, effects of cell deformation on viability are estimated using the experimental correlation based on the data obtained by compressing cells between parallel plates. These results provide insight for optimal parameter ranges for maximal cell viability during printing. Finally the cell is modeled as a non-Newtonian fluid while other phases are assumed to be Newtonian. Oldroyd-B fluid is selected to reflect the viscoelasticity of the cell and some preliminary results are presented.

Keywords: Compound droplets, finite-difference/front-tracking, Oldroyd-B fluid

ÖZET

Bu tezde, bir birleşik viskoz damlacığın düz bir zemine çarpma ve bu yüzeyde yayılması problemi, sonlu-farklar/arayüz-izleme metoduyla incelenmiştir. Bu yöntem, damlacık içerisine koyulan biyolojik hücrenin ink-jet yazıcı teknolojisi ile bir yüzeye yazılmasıyla 2 ve 3 boyutlu dokuların oluşturulmasını sağlamaktadır. Yöntemin başarısı hücrenin yazım sırasında hayatta kalmasına bağlıdır. Bu ise sıvı ile kaplanmış hücrenin çarpma dinamiğinin derinlemesine anlaşılmasını gerektirir. Bu çalışma, damlacık içerisine koyulan biyolojik hücrenin düz bir katı yüzeye yazılmasını sayısal olarak modellemenin ilk adımı mahiyetindedir. Hücre, hücreyi çevreleyen akışkan ve dış ortam Newtonsal akışkanlar olarak modellenmiştir. Hücrenin yaşamasının hücre deformasyonu ve deformasyon oranına bağlı olduğu varsayılmıştır. Boyutsuz sayıların hücreyi temsil eden iç damlacığın deformasyonu ve deformasyon hızı üzerindeki etkilerini incelemek üzere simülasyonlar gerçekleştirilmiştir. İçteki damlacık üzerindeki deformasyon; Reynolds sayısındaki artış, dıştaki damlacığın hücrenin yarıçapına oranındaki azalma, hava-dıştaki damlacık ve dıştaki damlacık-hücre arayüzlerindeki yüzey gerilmeleri oranındaki artış, hücre viskozitesinin dıştaki damlacığın viskozitesine oranındaki düşüş, dıştaki damlacığın zemin ile yaptığı statik kontak açısındaki azalma durumlarda artış göstermektedir. Ayrıca maksimum deformasyonun Weber sayısının 2 değeri civarında minimum olduğu gözlenmiştir. Hücrenin yaşama olasılığı paralel plakalar arasında hücrelerin sıkıştırılması ile elde edilen korelasyon kullanılarak hesaplanmıştır. Elde edilen sonuçlar, doku oluşturma sürecinde hücrenin yaşayabilirliği için optimal değerlerin öngörülmesini kolaylaştırmaktadır. Son bölümde ise, hücre Newtonsal olmayan bir akışkan olarak modellenerek hücrenin viskoelastik yapısı temsil edilmiştir. Bu durumda, hücre için Oldroyd-B Newtonsal olmayan akışkanı kullanılırken, hücreyi kaplayan damlacık ve dış ortam Newtonsal akışkanlar olarak modellenmiştir.

Anahtar Kelimeler: Birleşik damlacık, sonlu-farklar/arayüz-izleme, Oldroyd-B akışkanı

ACKNOWLEDGEMENTS

First I would like to thank my advisor Prof. Muradođlu who always guided me in my studies, oriented me to the area of fluid mechanics and helped me to merge my mathematics knowledge with fluid mechanics.

I am also grateful to the members of my thesis committee for their criticism and valuable comments.

I would like to thank my colleague Savař Tařođlu for his support and guidance during my study in Koc University.

Many thanks due to Onur Demir for his patience, motivation and support he provided me. I also would like to thank my friends zge Ekemen and Sercan Irmak who were always there for me. I would like to thank my friends Mge Karaman, Gzde Eskici, Emre Bıyıklı, Senem Gler, Erdem Cerit and Musa zboyacı whose friendships have made my two years in Koc University precious and memorable.

Finally and most importantly, I would like to thank my parents Meral and Cengiz Kaynak for the love and care they provided all my life. All these would not be possible without them.

TABLE OF CONTENTS

List of Tables	viii
List of Figures	ix
Nomenclature	xii
Chapter 1: Introduction	1
Chapter 2: Newtonian Fluid Model	5
2.1 Formulation and Numerical Method	5
2.2 Results and Discussion	10
2.2.1 Validation.	10
2.2.2 Impact and Spreading of a Compound Droplet	16
Chapter 3: Conclusions	32
Appendix A: Non-Newtonian Fluid Model	34
Bibliography	42
Vita	49

LIST OF TABLES

3.1	List of cases used for validation.	13
3.2	Density and viscosity values of three phases	18
3.3	Viabilities of cells	31

LIST OF FIGURES

2.1	Schematic illustration of the computational setup	7
2.2	Schematic illustration of the computational setup for slip contact line method	8
2.3	The normalized static droplet height versus Eötvös number in the range $Eo = 0.01$ and $Eo = 64$. Solid and dashed lines denote the analytical solutions for the limiting cases of $Eo \ll 1$ and $Eo \gg 1$, respectively. The inset shows the initial conditions for the droplet relaxation test	12
2.4	Time evolution of the spread factor of simple glycerin droplet spreading on the wax substrate	13
2.5	(a) The sketch for buoyancy driven compound droplet. (b) Comparison of the compound drop shapes obtained computationally by the present method (right) and experimentally by Mori (1978) (left). The dimensionless parameters are $Re = 0.016$; $Eo = 2.11$; $\rho_d/\rho_o = 1.29$; $\mu_d/\mu_o = 0.84$; $\sigma_i/\sigma_o = 3.64$; $d_i/d_o = 0.87$	14
2.6	Shape evolution of compound droplet at times $t_* = 0; 1; 4; 2; 4; 3; 5$ for $Re = 1; 2; 5$; $Eo = 180$; $\rho_d/\rho_o = 1.11$; $\mu_d/\mu_o = 0.5$; $\sigma_i/\sigma_o = 10$; $d_i/d_o = 0.75$. The present results (solid lines on the right side) are compared with those of Bazhlekov et al. (1995) (dashed lines on the left side).	15
2.7	The velocities of the top and bottom points of the compound drop at $Re = 1; 2; 5$; $Eo = 180$; $\rho_d/\rho_o = 1.11$; $\mu_d/\mu_o = 0.5$; $\sigma_i/\sigma_o = 10$; $d_i/d_o = 0.75$. The present results (solid lines) are compared with the results of Bazhlekov et al. (1995) (dashed lines)	16
2.8	Evolution of compound droplet impacting on a flat surface ([left half] pressure	

- contours and [right half] pressure distribution on the surface of the cell). Time evolves from left to right and from top to bottom, and the snapshots are taken at times $t^* = 0.000269, 0.0541, 0.1351, 0.2162, 0.2703, 0.135, 1.0270$ and 3.8432 . (We = 0.5, Re = 30, $d_o/d_i = 2.85, \sigma_o/\sigma_i = 2541, \mu_c/\mu_d = 10$) 19
- 2.9 Evolution of compound droplet impacting on a .at surface ([left half] velocity vectors and [right half] shear contours). Time evolves from left to right and from top to bottom, and the snapshots are taken at timest $t^* = 0.000269, 0.0541, 0.1351, 0.2162, 0.2703, 0.135, 1.0270$ and 3.8432 . (We = 0.5, Re = 30, $d_o/d_i = 2.85, \sigma_o/\sigma_i = 2541, \mu_c/\mu_d = 10$) 20
- 2.10 (a) Spread factor and (b) dynamic contact angle versus non-dimensional time for Re = 15, 20, 30, 40 and 45. (We = 0.5, $d_o/d_i = 2.85, \sigma_o/\sigma_i = 2541, \mu_c/\mu_d = 10$) 22
- 2.11 Deformation versus non-dimensional time for Re = 15, 20, 30, 40 and 45. (We = 0.5, $d_o/d_i = 2.85, \sigma_o/\sigma_i = 2541, \mu_c/\mu_d = 10$) 22
- 2.12 (a) Spread factor and (b) dynamic contact angle versus non-dimensional time for We = 0.25, 0.5, 1.0, 2.0, 5.0 and 10.0. (Re = 30, $d_o/d_i = 2.85, \sigma_o/\sigma_i = 2541, \mu_c/\mu_d = 10$) 23
- 2.13 (a) Deformation and (b) rate of deformation versus non-dimensional time for We = 0.25, 0.5, 1.0, 2.0, 5.0 and 10.0. (Re = 30, $d_o/d_i = 2.85, \sigma_o/\sigma_i = 2541, \mu_c/\mu_d = 10$) 23
- 2.14 (a) Spread factor and (b) dynamic contact angle versus non-dimensional time for $d_o/d_i = 1.5, 2.0, 2.5, 2.85, 3.0$ and 3.5 . (We = 0.5, Re = 30, $\sigma_o/\sigma_i = 2541, \mu_c/\mu_d = 10$) 24
- 2.15 Deformation and rate of deformation versus non-dimensional time $d_o/d_i = 1.5, 2.0, 2.5, 2.85, 3.0$ and 3.5 . (We = 0.5, Re = 30, $\sigma_o/\sigma_i = 2541, \mu_c/\mu_d = 10$) 25
- 2.16 (a) Spread factor and (b) dynamic contact angle versus non-dimensional time for $\sigma_o/\sigma_i = 10, 20, 50, 500, 2541$ and 5000 . (We = 0.5, Re = 30, $\mu_c/\mu_d = 10,$

	$d_o/d_i=2.85$)	26
2.17	Deformation and rate of deformation versus non-dimensional time for $\sigma_o/\sigma_i = 10$, 20, 50, 500, 2541 and 5000. (We = 0.5, Re = 30, $\mu_c/\mu_d = 10$, $d_o/d_i=2.85$)	26
2.18	(a) Spread factor and (b) dynamic contact angle versus non-dimensional time for $\mu_c/\mu_d=2, 5, 10, 20$ and 40. (We = 0.5, Re = 30, $d_o/d_i=2.85$, $\sigma_o/\sigma_i = 2541$)	27
2.19	Deformation and rate of deformation versus non-dimensional time for $\mu_c/\mu_d = 2, 5, 10, 20$ and 40. (We = 0.5, Re = 30, $d_o/d_i=2.85$, $\sigma_o/\sigma_i = 2541$)	27
2.20	(a) Spread factor and (b) dynamic contact angle versus non-dimensional time for $\theta_e = 30^\circ, 45^\circ, 60^\circ, 75^\circ, 90^\circ, 105^\circ$ and 120° (We = 0.5, Re = 30, $d_o/d_i=2.85$, $\sigma_o/\sigma_i = 2541$, $\mu_c/\mu_d=10$)	28
2.21	Deformation and rate of deformation versus non-dimensional time for $\theta_e = 30^\circ, 45^\circ, 60^\circ, 75^\circ, 90^\circ, 105^\circ$ and 120° (We = 0.5, Re = 30, $d_o/d_i=2.85$, $\sigma_o/\sigma_i = 2541$, $\mu_c/\mu_d=10$)	29
2.22	Evolution of compound droplet. (We = 0.5, Re = 30, $d_o/d_i=2.85$, $\sigma_o/\sigma_i = 2541$, $\mu_c/\mu_d=10$)	30
A.1	Comparison of Oldroyd-B and Newtonian Codes for the Newtonian Case at $t^*=0.0670; 0.2690; 0.6725$ and 1.3450 . (Time evolves from left to right and from top to bottom) (Left side of the plot represents solution with Oldroyd-B code, right side represents Newtonian solution)	39
A.2	Contact angle versus time for We = 0.5, Re = 30, $d_o/d_i=2.85$, $\sigma_o/\sigma_i = 2541$, $\mu_c/\mu_d=10$, and $\theta_e = 90^\circ$	40
A.3	Spread factor versus time for We = 0.5, Re = 30, $d_o/d_i=2.85$, $\sigma_o/\sigma_i = 2541$, $\mu_c/\mu_d=10$, and $\theta_e = 90^\circ$	40
A.4	Deformation versus time for We = 0.5, Re = 30, $d_o/d_i=2.85$, $\sigma_o/\sigma_i = 2541$, $\mu_c/\mu_d=10$, and $\theta_e = 90^\circ$	41

NOMENCLATURE

FD/FT	Finite-difference/Front-tracking
\mathbf{u}	velocity
p	pressure
ρ_o	density of the ambient fluid
ρ_d	density of the encapsulating fluid
ρ_c	density of the inner fluid
t	physical time
t^*	non-dimensional time
σ	surface tension
κ	curvature
\mathbf{x}	location of a front point
\mathbf{x}_f	location of the front
I	indicator function
μ	viscosity
μ_s	solvent viscosity
μ_p	polymeric viscosity
λ	relaxation time

Chapter 1

INTRODUCTION

Impingement of a micro-droplet on a flat surface has important applications in engineering such as surface coating, spray cooling, DNA microarrays, and ink-jet printing [1]. The impact and spreading of a homogenous one-component (simple) liquid droplet on a flat surface have been studied extensively in the literature from theoretical [2, 3, 4, 5], computational [6, 7, 8, 9, 10] and experimental [4, 11, 12, 13] points of view. In spite of a growing interest in generation and manipulation of multi-component (compound) droplets mainly driven by microfluidic applications [14, 15, 16] in recent years, to the best of our knowledge, no work has been done on the impingement of a compound droplet on a solid surface except for the experimental study of Chen et al. [15]. They formed compound droplets consisting of water as the inner droplet and diesel oil as the encapsulating fluid and studied the residence time of a compound droplet impinging on a hot surface to understand the heat transfer process in spray combustion [15]. The impingement of a compound droplet is of fundamental importance in fluid mechanics. Here, we draw inspiration from the recent experimental cell printing studies where live cell encapsulating droplets are patterned onto biomaterial coated substrates to engineer 3D tissue constructs [17, 18, 19, 20, 21], or to cryopreserve cells [18, 22, 23]. The current droplet generation technologies make it possible to generate monodispersed droplets on demand with specified size such that the droplets can encapsulate only single to few cells and deposit them with spatial control on a substrate [18]. This suggests that it would be useful to model the process computationally to predict optimal conditions enhancing cell viability.

Fundamental studies of the dynamics of compound droplets have been done relatively recently compared to the simple droplets [24] and there are still fundamental questions that need to be addressed [14, 25]. Compound droplets have found important applications in targeted drug delivery [26, 27], food industry [28], waste water management [29]

and microfluidics [14]. Fluid mechanics of compound droplets have been studied in various geometries and flow conditions. Johnson and Sadhal [24] reviewed the translation of compound droplets in quiescent flow. Stone and Leal [30] studied the breakup of double emulsion droplets in extensional flows. Bazhlekov et al. [31] examined the unsteady motion and deformation of compound droplets rising in an otherwise quiescent fluid due to buoyancy using a finite element method. Smith et al. [25] investigated the deformation and breakup of an encapsulated droplet in shear flow using a level-set method and produced a range of morphologies caused by the interaction between the core and outer interfaces. They presented a phase diagram showing the morphologies obtained for a range of capillary numbers and core interfacial tensions. Kawano et al. [32] studied deformations of thin liquid spherical shells in liquid-liquid-gas system both experimentally and computationally. In recent years, the field has been mainly driven by a growing range of applications in microfluidics. Utada et al. [14] developed a micro capillary device that generates double emulsions at specified sizes and numbers. This capillary device forms monodisperse double emulsions in one step. Zhou et al. [33] computationally studied the formation of compound drops in flow-focusing devices and found that compound drops are formed only in a narrow window of flow and rheological parameters.

Modeling cells as simple Newtonian droplet is not new and has been widely used to study blood cells [34, 35, 36, 37]. In these models, the cell is represented by a Newtonian droplet whose viscosity is much higher than that of ambient fluid. The Newtonian models involve oversimplification as they ignore the complicated internal structure of the cells and lump the effects of the internal structure into the *apparent* viscosity usually measured by the micropipet aspiration technique [38, 39]. A compound droplet has been proposed by Kan et al. [40] as a model for leukocyte deformation in an imposed extensional flow and by Marella and Udaykumar [41] as a model for leukocyte deformability in micropipet aspiration and recovery phases. In these models, the inner droplet represents the nucleus of the cell while the encapsulating droplet represents the cytoplasm. Kan et al. [40] treated both the nucleus and cytoplasm as Newtonian fluids with different material properties. Marella and Udaykumar [41] improved this model using a power-law shear thinning fluid for the cytoplasm and an elastic membrane with non-linear stress-strain curve for the cortical layer.

To the best of our knowledge, only computational modeling of the cell-encapsulating

droplet printing has been performed by Wang et. al. [42] using a smoothed particle hydrodynamics (SPH) method. They assumed that the receiving substrate is coated by the same liquid as that encapsulating the cell. Therefore, the fluid mechanical problem they considered is fundamentally different from that which we study here.

In the present work, the impact and spreading of a compound droplet are studied computationally using a front-tracking/finite-difference method [43] as a model for the cell-encapsulating droplet printing on a flat solid substrate. In the present model, the cell, the encapsulating liquid and surrounding air are first assumed to be Newtonian fluids with different material and interfacial properties. This is called all-Newtonian model. In this model, the inner droplet is composed of a highly viscous Newtonian fluid representing the cell. This is, of course, an oversimplification, as the cell is not a Newtonian droplet. However, we use this rather simple model to facilitate extensive simulations. It is assumed that the cell-encapsulating droplet partially wets the substrate while the inner droplet is non-wetting. Note that, as far as the computational method is concerned, there is no difficulty to allow the inner droplet to wet the substrate but we simply postulate that the cell does not wet or stick to the substrate. The present front-tracking method developed by Unverdi and Tryggvason [44] has been recently extended to treat the moving contact lines and successfully applied to model the impact and spreading of a simple droplet by Muradoglu and Tasoglu [45]. In this method, the stress singularity at the contact line is removed by moving the contact line such that the contact angle is equivalent to the dynamic contact angle that is computed at every time step using the correlation given by Kistler [46]. Finally the compound droplet model is extended to treat the biological cell as a non-Newtonian fluid. The Oldroyd-B fluid is selected to reflect the viscoelastic behavior of the biological cell and some preliminary results are presented at the end of the thesis. However, a detailed study of non-Newtonian or microstructured models is deferred to future work.

To enable commercial implementation of the cell printing technology in the health care industry, approaches need to minimize the cell damage occurring during impact/collision with the receiving substrate. It is known that cell viability is strongly correlated with cell deformation [47]. Lower levels of cell deformation is more likely to enhance survival during the collision. We also hypothesize that the rate of cell deformation is also important in cell viability. Therefore, the goal here is to identify the conditions that yield the smallest cell

deformation and deformation rate. For this purpose, effects of relevant non-dimensional numbers such as the Reynolds number, the Weber number, the viscosity ratio, the surface tension ratio, the diameter ratio and the equilibrium contact angle on the cell deformation and deformation rate are investigated. The cell viability is related to the cell deformation using the experimental data obtained from the compression of cells by two parallel plates [47].

The paper is organized as follows: The mathematical formulation and numerical model are described and results are presented for the Newtonian model in the next chapter. In Chapter 3, we represent conclusions for. Finally, the non-Newtonian fluid model is introduced and some preliminary results are presented in Appendix A.

Chapter 2

NEWTONIAN FLUID MODEL

2.1 Formulation and Numerical Method

The flow equations are described here in the context of the finite-difference/front-tracking (FD/FT) method. The fluid motion is assumed to be governed by the incompressible Navier-Stokes equations. We solve for the flow inside and outside the droplets in all three phases. Following Unverdi and Tryggvason [44], a single set of governing equations can be written for the entire computational domain, provided that the jumps in material properties such as density and viscosity are correctly accounted for, and surface tension is included. In an axisymmetric coordinate system, the Navier-Stokes equations in conservative form are given by

$$\begin{aligned}
\frac{\partial \rho u}{\partial t} + \frac{1}{r} \frac{\partial r \rho u^2}{\partial r} + \frac{\partial \rho u v}{\partial z} &= -\frac{\partial p}{\partial r} + \frac{\partial}{\partial r} \left(2\mu \frac{\partial u}{\partial r} \right) + 2\mu \frac{\partial}{\partial r} \left(\frac{u}{r} \right) + \frac{\partial}{\partial z} \mu \left(\frac{\partial v}{\partial r} + \frac{\partial u}{\partial z} \right) \\
&\quad - \int_A \sigma \kappa \mathbf{n} \delta(\mathbf{x} - \mathbf{x}_f) d\mathbf{A} \cdot \hat{\mathbf{i}}_r, \\
\frac{\partial \rho v}{\partial t} + \frac{1}{r} \frac{\partial r \rho u v}{\partial r} + \frac{\partial \rho v^2}{\partial z} &= -\frac{\partial p}{\partial z} + \frac{\partial}{\partial r} \mu r \left(\frac{\partial v}{\partial r} + \frac{\partial u}{\partial z} \right) + \frac{\partial}{\partial z} \left(2\mu \frac{\partial v}{\partial z} \right) - \Delta \rho g \\
&\quad - \int_A \sigma \kappa \mathbf{n} \delta(\mathbf{x} - \mathbf{x}_f) d\mathbf{A} \cdot \hat{\mathbf{i}}_z,
\end{aligned} \tag{2.1}$$

where u and v are the velocity components in the radial and axial directions, p is the pressure, g is the gravitational acceleration, and ρ and μ are the discontinuous density and viscosity fields, respectively. The effect of surface tension is included as a body force shown in the last term on the right hand side, where σ is the surface tension, κ is twice the mean curvature, and \mathbf{n} is a unit vector normal to the interface. The surface tension acts only on the interface as indicated by the three-dimensional delta function δ whose arguments \mathbf{x} and \mathbf{x}_f are the point at which the equation is evaluated and a point at the interface, respectively. The Navier-Stokes equations are supplemented by the incompressibility condition

$$\frac{1}{r} \frac{\partial r u}{\partial r} + \frac{\partial v}{\partial z} = 0.$$

We also assume that the material properties remain constant following a fluid particle, i.e., $D\rho/Dt = 0$ and $D\mu/Dt = 0$, where D/Dt is the material derivative. The density and viscosity vary discontinuously across the interfaces and are given by

$$\begin{aligned} \rho &= \begin{cases} \rho_d I(r, z, t) + \rho_o(1 - I(r, z, t)) & \text{If } I(r, z, t) \leq 1.0 \\ \rho_c(I(r, z, t) - 1) + \rho_d(2 - I(r, z, t)) & \text{Otherwise} \end{cases} \\ \mu &= \begin{cases} \mu_d I(r, z, t) + \mu_o(1 - I(r, z, t)) & \text{If } I(r, z, t) \leq 1.0 \\ \mu_c(I(r, z, t) - 1) + \mu_d(2 - I(r, z, t)) & \text{Otherwise} \end{cases} \end{aligned} \quad (2.2)$$

where the subscripts “c”, “d” and “o” denote properties of the inner droplet, encapsulating droplet and the ambient fluid, respectively, and $I(r, z, t)$ is the indicator function defined as

$$I(r, z, t) = \begin{cases} 2 & \text{in inner droplet,} \\ 1 & \text{in outer droplet,} \\ 0 & \text{in bulk fluid.} \end{cases}$$

The numerical method is based on the front-tracking/finite-difference method developed by Unverdi and Tryggvason [44]. In this method, a separate Lagrangian grid is used to track the droplet-droplet and droplet-ambient fluid interface. The Lagrangian grid consists of linked marker points (the front) that move with the local flow velocity that is interpolated from the stationary Eulerian grid as sketched in Fig. 2.1. The piece of the Lagrangian grid between two marker points is called a front element. The Lagrangian grid is used to find the surface tension, which is then distributed onto Eulerian grid points near the interface using Peskin’s cosine distribution function [48], and added to the momentum equations as body forces as described by Tryggvason et al. [43]. At each time step, the indicator function is computed and is used to set the fluid properties inside and outside the droplets. To do this, unit magnitude jumps are distributed in a conservative manner on the Eulerian grid points near the interfaces using the Peskin’s cosine distribution function [48] and are then integrated to compute the indicator function everywhere. The computation of the indicator function requires solution of a separable Poisson equation and yields a smooth transition of the indicator function across the interface. The fluid properties are then set as a function of the indicator function according to Eq. (2.2). The Lagrangian grid is restructured at every time step. This is done by deleting the front elements that are smaller than a specified lower limit and by splitting the front elements that are larger than a specified upper limit, in the

same way as described by Tryggvason et al. [43]. This maintains the front element size to be nearly uniform and comparable to the Eulerian grid size. Restructuring the Lagrangian grid is crucial because it avoids unresolved wiggles due to small elements and lack of resolution due to large elements. The details of the front-tracking method can be found in Unverdi and Tryggvason [44] and Tryggvason et al. [43].

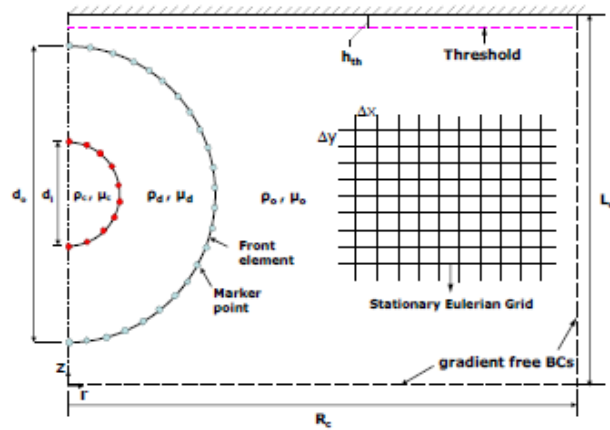


Figure 2.1: Schematic illustration of the computational setup.

The no-slip boundary condition yields a stress singularity near the contact line. Therefore it requires special treatment. The treatment of the contact line is essentially the same as that of Muradoglu and Tasoglu [45] so it is briefly summarized here for the compound droplet case. In the framework of the front-tracking method, the drop interface must be connected to the solid wall explicitly when the droplet approaches sufficiently close to the wall because the interface is tracked explicitly by marker points. For this purpose, we assume that the drop interface connects to the wall when the distance between the drop interface and solid wall is less than a prespecified threshold value h_{th} as shown in Fig. 2.2. To achieve this, the interface is continuously monitored during the simulation and the first front element crossing the threshold line is detected. Subsequently, this element is connected to the solid wall such that the contact angle between the wall and droplet is equal to the apparent contact angle θ_D . In the present work, the apparent contact angle is specified dynamically using Kistler's correlation [12, 46] that relates the apparent contact angle to the capillary number defined as $Ca_{cl} = \mu_d V_{cl} / \sigma$ where V_{cl} is the speed of the contact line.

Because Kistler's correlation is valid for small capillary numbers, following Muradoglu and Tasoglu [45], it is slightly modified as follows:

$$\theta_{Di} = f_{\text{Hoff}} \left(Ca_{clm} + f_{\text{Hoff}}^{-1}(\theta_e) \right), \quad (2.3)$$

where f_{Hoff}^{-1} is the inverse of the Hoffman's function f_{Hoff} defined as

$$f_{\text{Hoff}}(x) = \arccos \left\{ 1 - 2 \tanh \left[5.16 \left(\frac{x}{1 + 1.31x^{0.99}} \right)^{0.706} \right] \right\}. \quad (2.4)$$

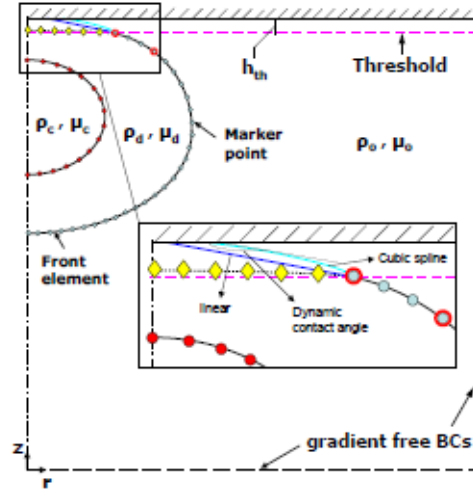


Figure 2.2: Schematic illustration of the computational setup for slip contact line method.

In Eq. (2.4), θ_e is the equilibrium (static) contact angle and Ca_{clm} is defined as $Ca_{clm} = \min(Ca_{max}, Ca_{cl})$ where Ca_{max} is the cut-off capillary number introduced to avoid too large or too small values of the apparent contact angle. The apparent contact angle is then determined in the advancing and receding phases as

$$\theta_D = \begin{cases} \theta_{Di} & \text{if } V_{cl} \geq 0 \text{ (advancing)} \\ 2\theta_e - \theta_{Di} & \text{if } V_{cl} < 0 \text{ (receding)}. \end{cases} \quad (2.5)$$

Following Muradoglu and Tasoglu [45], the contact line velocity is specified as the velocity of the point where the droplet interface crosses the threshold. This definition is found to be very robust. Once the apparent contact angle is determined, the front element crossing the

threshold line is connected to the solid wall as follows: First, the distance between the front element that is to be connected and the wall is predicted assuming that the front element connects to the wall linearly. If this distance is smaller than a prespecified threshold length, h_{th} , then the front element is connected to wall by fitting a cubic curve and imposing the dynamic contact angle as sketched in Fig. 2.2. Otherwise the front element is connected to the wall using a linear function and again imposing the dynamic contact angle on the wall. The threshold length is typically taken as $h_{th} = 2\Delta x$ where Δx is the Eulerian grid size. Note that we need three points for a cubic fit because one condition is imposed by the apparent contact angle. For this purpose, the first point is selected as the marker point on the front element crossing the interface and the other two are selected such that the distance between the selected marker points is approximately equal to the distance between the first marker point and the wall. Typical marker points used in cubic fit are schematically shown in Fig. 2.2 as large dots. After the front element on the threshold line is connected to the solid wall, the interface is restructured in a similar way as described by Tryggvason et al. [43]. In addition to specifying the contact angle dynamically as explained above, the dynamic contact angle is also used to compute the curvature at the center of the front element adjacent to the solid wall. Following Tryggvason et al. [43], the curvature is computed at the center of each front element and is approximated as a difference between the tangent vectors at the end points of the element. The tangent vectors are computed by fitting a cubic polynomial for the internal front elements. In the case of contact line, one marker point of the front element adjacent to the solid wall is placed on the wall so it requires a special treatment. The tangent at this marker point is simply set to the tangent of the dynamic contact angle given by Eq. (2.5). This procedure is found to be very robust and accurate. The details of the implementation of this slip contact method can be found in Muradoglu and Tasoglu [45].

The governing equations are solved in their dimensional forms, and the results are expressed in terms of relevant dimensionless quantities. Let \mathcal{L} and \mathcal{U} be appropriately defined length and velocity scales, respectively, and $\mathcal{T} = \mathcal{L}/\mathcal{U}$ be the time scale. Then the relevant dimensionless numbers can be summarized as

$$Re = \frac{\rho_d \mathcal{U} \mathcal{L}}{\mu_d}; \quad We = \frac{\rho_d \mathcal{U}^2 \mathcal{L}}{\sigma_o}; \quad \frac{d_o}{d_i}; \quad \frac{\sigma_o}{\sigma_i}; \quad \frac{\mu_c}{\mu_d}; \quad \frac{\mu_d}{\mu_o}; \quad \theta_e; \quad (2.6)$$

where Re is the Reynolds number, We is the Weber number, and d_i and d_o are the diameters of inner and outer droplets, respectively. The surface tension coefficients of the droplet-droplet interface, and droplet-ambient fluid interface are denoted by σ_i and σ_o , respectively.

2.2 Results and Discussion

2.2.1 Validation

The numerical method is first validated in this section. To the best of our knowledge, there is no experimental or computational study about the impact and spreading of a compound droplet on a substrate that we can use for validation of the present numerical method. The accuracy and convergence of the present numerical method have been recently demonstrated by Muradoglu and Tasoglu [45] for a simple droplet. Therefore, a comprehensive validation is not repeated here. Instead, emphasis is placed on the validation of the numerical method for the compound droplet case.

We first consider the relaxation of a compound viscous droplet from a spherical initial condition to its final equilibrium shape. For this test, a concentric spherical compound droplet of the inner radius R_i and the outer radius R_o is initialized near the solid surface as shown in the inset of Fig. 2.3 and is allowed to spread until its final static shape is reached for various values of the Eötvös number ($Eo = (\rho_d - \rho_o)gR_o^2/\sigma_o$) that represents the ratio of gravitational and surface tension forces. The inner and the encapsulating droplet densities are equal and larger than the surrounding fluid. The viscosities of the inner and encapsulating droplets are also set equal although viscosity does not have any effect on the final static shape of the droplet. Note that this test case becomes equivalent to the simple droplet case studied by Muradoglu and Tasoglu [45] when the ratio of surface tension coefficients is large, i.e., $\sigma_o/\sigma_i \gg 1$. The static shape of the droplet generally depends on the equilibrium contact angle θ_e , the Eötvös number and the ratio of surface tension coefficients. In the limit of vanishing Eötvös numbers, i.e., $Eo \ll 1$, the equilibrium shape of the droplet is determined by the surface tension force and the encapsulating droplet takes a shape of spherical cap with the maximum height of the droplet, H_o , given by [45]

$$H_o = R_o(1 - \cos \theta_e) \left(\frac{4}{2 + \cos^3 \theta_e - 3 \cos \theta_e} \right)^{1/3}. \quad (2.7)$$

On the other hand, when $Eo \gg 1$ and $\sigma_o/\sigma_i \gg 1$, the compound droplet becomes equivalent to the corresponding simple droplet and the shape of the droplet is controlled mainly by the competition between the gravitational and surface tension forces and, the maximum height of the droplet is proportional to the capillary length [45], i.e.,

$$H_\infty = \frac{2H_o \cos(\theta_e/2)}{\sqrt{Eo}}, \quad (2.8)$$

where H_o is given by Eq. (2.7). Computations are performed for this test case and the results are compared with the asymptotic solutions given by Eqs. (2.7) and (2.8). For this purpose, the equilibrium contact angle is set to $\theta_e = 93^\circ$ and the dynamic angle is used at the contact line. Focus here is placed on the static shape of the droplet. The computational domain extends 6.5 drop radii both in the axial and radial directions, and is resolved by a 256×256 uniform Cartesian grid. Figure 2.3 shows the normalized static droplet height as a function of Eötvös number for the ratio of surface tension coefficients together with the steady shapes of droplet in the range of $Eo = 0.01$ and 64. It is clearly seen that the computed normalized droplet height agrees well with the asymptotic solutions given by Eq. (2.7) and Eq. (2.8) for $Eo \ll 1$ and $Eo \gg 1$, respectively, when $\sigma_i/\sigma_o \ll 1$. For instance, the difference between the asymptotic solution and computational result is less than 0.2% for $Eo = 0.01$ and 10% for $Eo = 64$, respectively. We also note that the difference between the asymptotic solution and computational results decreases monotonically as Eötvös number increases. For the intermediate values of Eötvös number, the transition between a spherical cap and a puddle shape occurs. However, the numerical solution deviates significantly from the asymptotic solution for large Eötvös numbers as σ_i/σ_o increases since the inner droplet resists the gravitational forces and causes a bump as shown in Fig. 2.3.

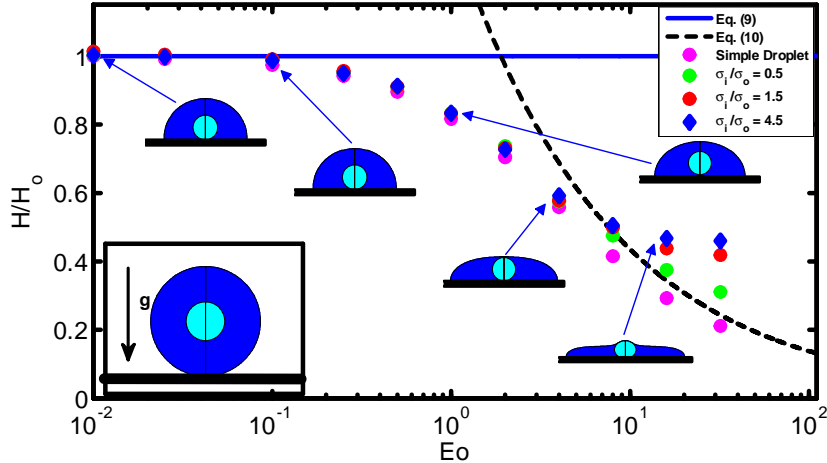


Figure 2.3: The normalized static droplet height versus Eötvös number in the range $Eo = 0.01$ and $Eo = 64$. Solid and dashed lines denote the analytical solutions for the limiting cases of $Eo \ll 1$ and $Eo \gg 1$, respectively. The inset shows the initial conditions for the droplet relaxation test.

Dynamics of the contact line is of fundamental importance for accurate simulation of impact and spreading of compound droplet. The treatment of contact line is essentially the same as that of Muradoglu and Tasoglu [45] and it has been extensively discussed for simple droplet case. Because there is no experimental or computational study about compound droplet spreading, the treatment of contact line is tested here for a simple droplet case studied experimentally by Sikalo et al. [12]. Only one set of results is shown here for completeness in Fig. 2.4. Detailed discussion of simple droplet case is conducted by Muradoglu and Tasoglu [45]. In this test case, the impact and spreading of simple glycerin droplet on a flat wax substrate is considered. The surrounding medium is air. The equilibrium contact angle is set to $\theta_e = 93^\circ$. Simulations are performed for three impact velocities as summarized in Table 2.1. As can be seen in Fig. 2.4, there is a good agreement between the computational and experimental results, i.e., the difference between the computational results and the experimental data is less than 10%. Considering the uncertainties in the experimental data and in the correlation used for dynamic contact angle, Fig. 2.4 indicates the accurate treatment of the contact line.

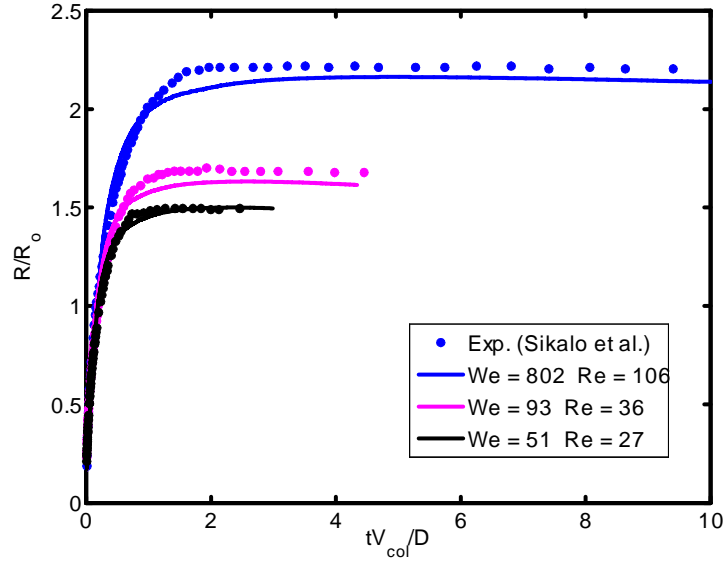


Figure 2.4 Time evolution of the spread factor of simple glycerin droplet spreading on the wax substrate.

Table 2.1: List of cases used for validation.

Cases	Liquid	Wall	Impact velocity (m/s)	We	Re	θ_e
1	Glycerin	Wax	4.1	802	106	93°
2	Glycerin	Wax	1.41	93	36	93°
3	Glycerin	Wax	1.04	51	27	93°

The final validation test deals with buoyancy-driven motion of compound droplet studied experimentally by Mori [49] and computationally using a finite element method by Bazhlevkov et al. [31]. As shown in Fig. 2.5a, an initially concentric gas-liquid compound droplet (the inner phase is a gas) rises due to buoyancy in an infinite domain. In addition to the dimensionless hydrodynamic parameters given by Eq. (2.6), the problem also depends on the Eötvös number defined here as $Eo = g\mathcal{L}^2\rho_o/\sigma_o$. Following Bazhlevkov et al. [31], the length and velocity scales are defined here as $\mathcal{L} = R_o$ (where $R_o = d_o/2$) and $\mathcal{U} = 2R_o^2\rho_o g/9\mu_o$. Then the time scale is given by $\mathcal{T} = \mathcal{L}/\mathcal{U}$. The flow is assumed to be axisymmetric. The computational domain extends 5 and 15 droplet radii in the radial and axial directions,

respectively, and is resolved by 256×768 uniform Cartesian grid. The computational results are first compared with the experimental data of Mori [49] in Fig. 2.5b. For this case, the dimensionless parameters are set to $Re = 0.016$, $EO = 2.11$, $\rho_d/\rho_o = 1.29$, $\mu_d/\mu_o = 0.84$, $\sigma_i/\sigma_o = 3.64$, $d_i/d_o = 0.87$. As can be seen in Fig. 2.5b, there is a good agreement between the experimental and computational droplet shapes. We next compare the present computational results with the finite element simulations of Bazhlekov et al. [31]. For this purpose, the computations are performed for the non-dimensional parameters of $Re = 1.25$, $EO = 180$, $\rho_d/\rho_o = 1.11$, $\mu_d/\mu_o = 0.5$, $\sigma_i/\sigma_o = 10$, $d_i/d_o = 0.75$. The droplet shapes are plotted in Fig. 2.6 at times $t^* = 0, 1.4, 2.4$ and 3.5 together with the results of Bazhlekov et al. [31]. This figure shows that there is a qualitatively good agreement between the present results and finite element simulations. The results are then quantified in Fig. 2.7 where the normalized velocities of the top and bottom points of the compound droplet are plotted as a function of dimensionless time. The velocity of top point is slightly overpredicted by the present method, but there is overall good agreement with the finite element simulations. Note that Kawano et al. [50] reported small-amplitude oscillations of encapsulated liquid interfaces especially just after the compound droplet is generated at the tip of injection nozzle. We have not observed any such oscillations of encapsulated drop interfaces for the cases studied in this section probably due to the fact that the droplet production period is not considered and focus is placed on the steady motion in the present study. We also note that neither Mori [49] nor Bazhlekov et al. [31] reported any oscillatory behavior of encapsulating drop interfaces.

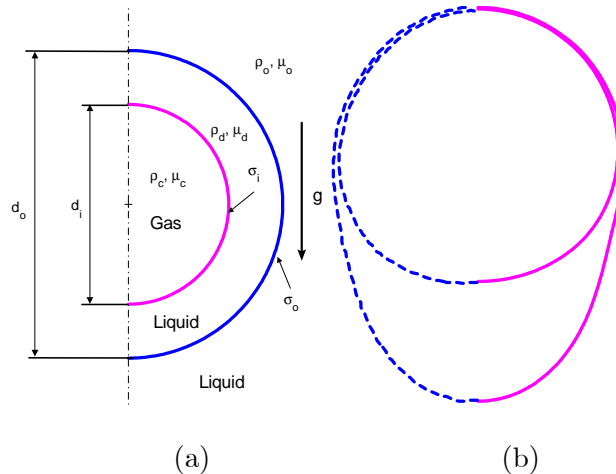


Figure 2.5: (a) The sketch for buoyancy driven compound droplet. (b) Comparison of the compound drop shapes obtained computationally by the present method (right) and experimentally by Mori (1978) (left). The dimensionless parameters are $Re = 0.016$, $EO = 2.11$, $\rho_d/\rho_o = 1.29$, $\mu_d/\mu_o = 0.84$, $\sigma_i/\sigma_o = 3.64$, $d_i/d_o = 0.87$.

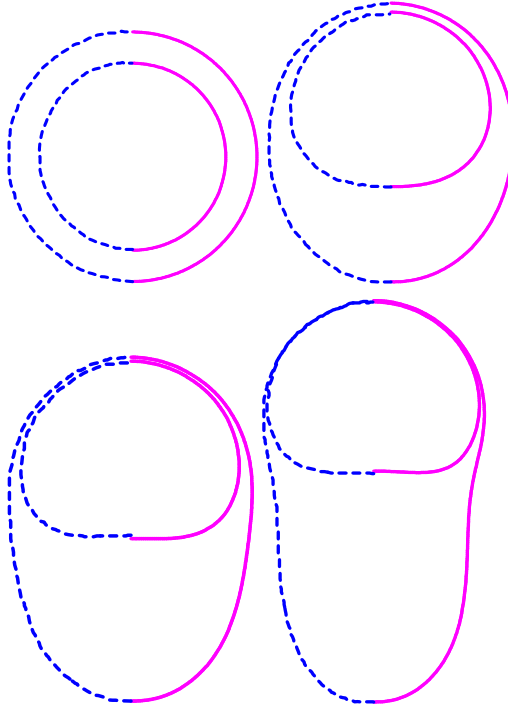


Figure 2.6: Shape evolution of compound droplet at times $t^* = 0, 1.4, 2.4, 3.5$ for $Re = 1.25$, $EO = 180$, $\rho_d/\rho_o = 1.11$, $\mu_d/\mu_o = 0.5$, $\sigma_i/\sigma_o = 10$, $d_i/d_o = 0.75$. The present results (solid lines on the right side) are compared with those of Bazhlekov et al. (1995) (dashed lines on the left side).

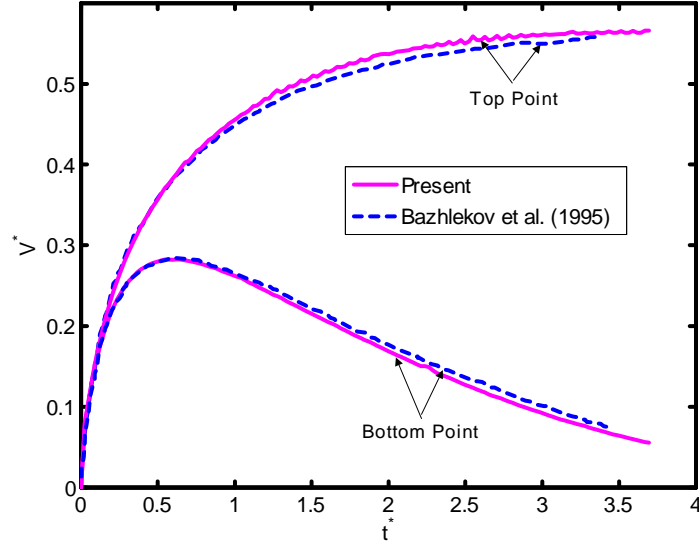


Figure 2.7: The velocities of the top and bottom points of the compound drop at $Re = 1.25$, $Eo = 180$, $\rho_d/\rho_o = 1.11$, $\mu_d/\mu_o = 0.5$, $\sigma_i/\sigma_o = 10$, $d_i/d_o = 0.75$. The present results (solid lines) are compared with the results of Bazhlekov et al. (1995) (dashed lines).

2.2.2 Impact and Spreading of a Compound Droplet

After validating the numerical method in the previous section, we now present simulations of compound droplet spreading on a flat substrate. The computational setup is sketched in Fig. 2.1. Computational domain extends approximately 6 outer drop radii in radial direction and 3 drop radii in axial direction and it is resolved by 512×256 uniform Cartesian grid in all the results presented in this section unless specified otherwise. An extensive grid convergence study of the present numerical method has been performed by Muradoglu and Tasoglu [45] for a simple droplet case. Therefore, such a study is not repeated here. However, grid convergence is checked for all the results presented, and we ensured that the solutions are grid independent, i.e., the spatial error is below 5%.

In the experimental study of Demirci and Mostaseno [18], the diameters of the encapsulating droplet and the cell are $d_o = 37\mu m$ and $d_i = 13\mu m$ (RAJI cell), respectively ($d_o/d_i = 2.85$). The cells are encapsulated in the 8.5% sucrose and 0.3% dextrose solution with density $\rho_d = 1030 \text{ kg/m}^3$ and viscosity of $\mu_d = 1.27 \times 10^{-3}$. In the simulations, the material properties of the solution encapsulating the cell are set to its physical values. The

density of the inner cell is set equal to that of the encapsulating droplet due to large amount of water content of the cell. There is no known exact value for the viscosity of RAJI cell, or for any cell in general, owing to its microstructured composition, but it can be assumed to be a highly viscous fluid. The viscosity of cell is taken here as an order of magnitude larger than that of the encapsulating droplet mainly due to numerical purposes in spite of the fact that actual apparent viscosity of the cell is much higher. For the same reason, the density of the surrounding air is also set to $\rho_o = 51.5 \text{ kg/m}^3$ that is about 40 times larger than its physical value. The material properties used in the simulations are summarized in Table 2.2 for all three phases. Surface tension at the air-solution interface and the solution-cell interface are 0.07622 and 0.00003 N/m , respectively ($\sigma_o/\sigma_i = 2541$). Note that the surface tension at the air-solution interface is based on the experimental data provided by Hoorfar et al. [51]. We assume that the solution remains homogeneous throughout so that the surface tension at the air-solution interface is constant. Based on the experimental data and considerations for numerical stability and convergence, we choose the set of the dimensionless numbers $We = 0.5$, $Re = 30$, $d_o/d_i = 2.85$, $\sigma_o/\sigma_i = 2541$, $\mu_c/\mu_d = 10$, $\mu_d/\mu_o = 40$, $\rho_c/\rho_d = 1$, $\rho_d/\rho_o = 20$ and $\theta_e = 90^\circ$ as the base case. Then, we study the effects of each non-dimensional number by systematically varying its value while keeping the other parameters the same as the base case. Note that the density and viscosity ratios between the encapsulating liquid and air are an order of magnitude larger in the experiment. However, it is found that a further increase in the property ratios does not effect the computational results significantly (not shown here). The compound droplet is initially located close to the wall, and initiated with a uniform (impact) velocity directed toward the wall. The equilibrium contact angle is chosen as 90° unless stated otherwise. Note that this static contact angle is much larger than the value in the experimental study, i.e., the static contact angle in the experimental work is about 10° . We choose a larger contact angle because it is computationally expensive to resolve the thin liquid layer close to the solid surface for small contact angles. We first present the simulations for the base case. Figure 2.8 shows snapshots of the collision taken at times $t^* = 0.000269, 0.0541, 0.135, 0.216, 0.270, 0.514, 1.027$ and 3.843 . In this figure, pressure contours are plotted on the left side, and pressure distribution on the cell surface is plotted on the right side of the droplet images. For the same parameters, velocity vectors (left side) and shear stress contours

Table 2.2: Density and viscosity values of three phases

Fluids	Density (kg/m^3)	Viscosity ($Pa\cdot s$)
Surrounding fluid	51.5	3.175e-05
Solution encapsulating the cell	1030	1.270e-03
RAJI cell	1030	1.270e-02

(right side) are plotted in Fig. 2.9. Shear stress reaches its peak value near the contact line at the beginning of collision and it consistently decreases while the compound droplet is spreading. Even at the beginning of droplet impact, the magnitude of the shear stress is nearly half of the maximum pressure. It is observed that the maximum shear stress occurs at the solution-air interface since all fluid particles within the compound droplet initially have the same velocity while the air is initially quiescent, and thus the velocity gradient is larger at the solution-air interface rather than at the cell-solution interface. Negative shear stress occurs in the vicinity of the contact line where both velocity and pressure gradients are extremely large and there is a stagnation-point like flow field. It is emphasized here that it is very likely that the numerical error is also large near the contact line due to large pressure and velocity gradients. The location of maximum pressure changes during the different phases of the collision process. For example, pressure increases near the contact line during the initial impact and spreading period; also just prior to recoil, the maximum pressure is located near the triple point. However, the pressure maximum starts to shift towards the distal point from the wall, where it remains until the recoil phase.

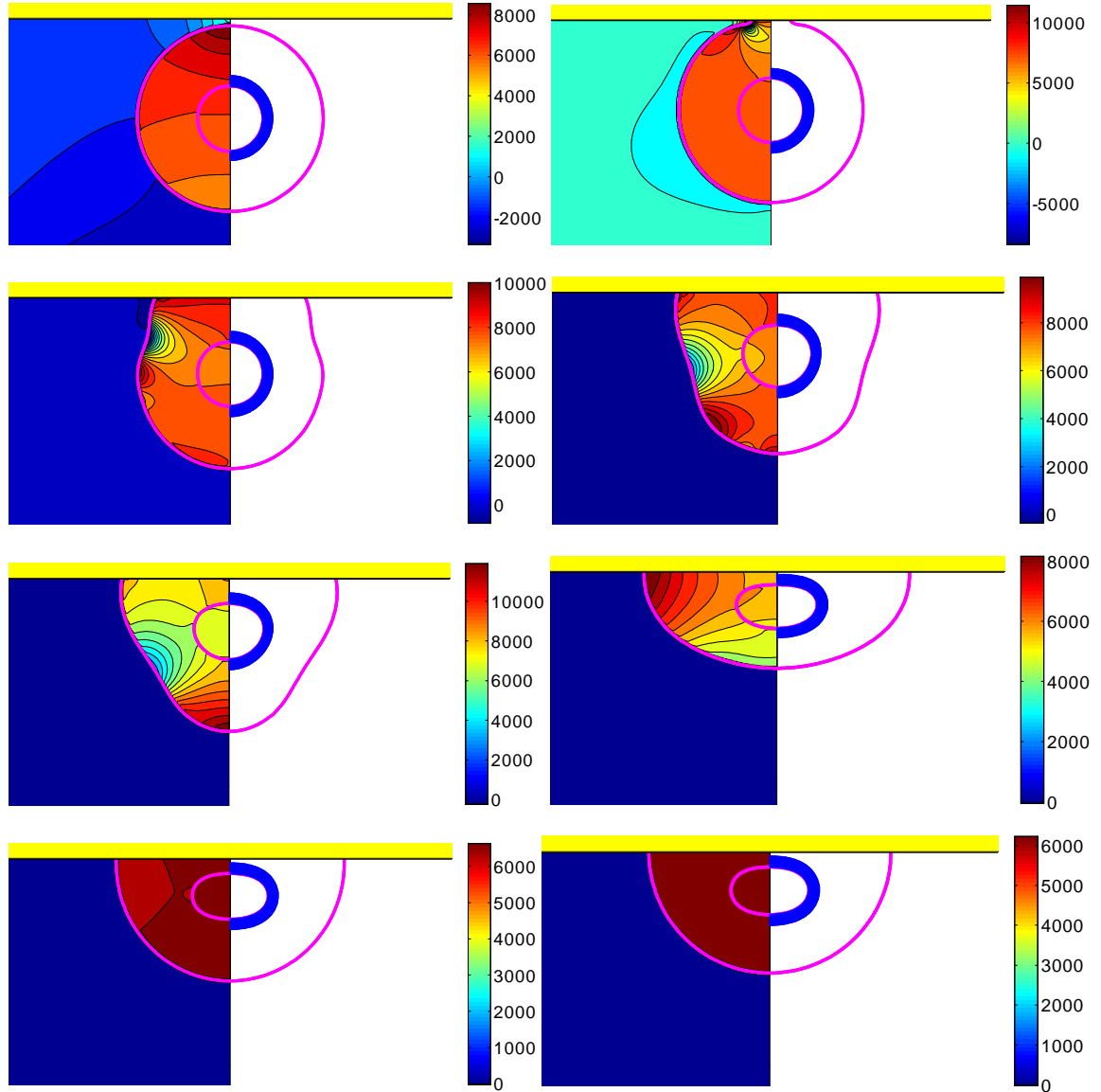


Figure 2.8: Evolution of compound droplet impacting on a flat surface ([left half] pressure contours and [right half] pressure distribution on the surface of the cell). Time evolves from left to right and from top to bottom, and the snapshots are taken at times $t^* = 0.000269, 0.0541, 0.1351, 0.2162, 0.2703, 0.5135, 1.0270$ and 3.8432 . ($We = 0.5, Re = 30, d_o/d_i = 2.85, \sigma_o/\sigma_i = 2541, \mu_c/\mu_d = 10$).

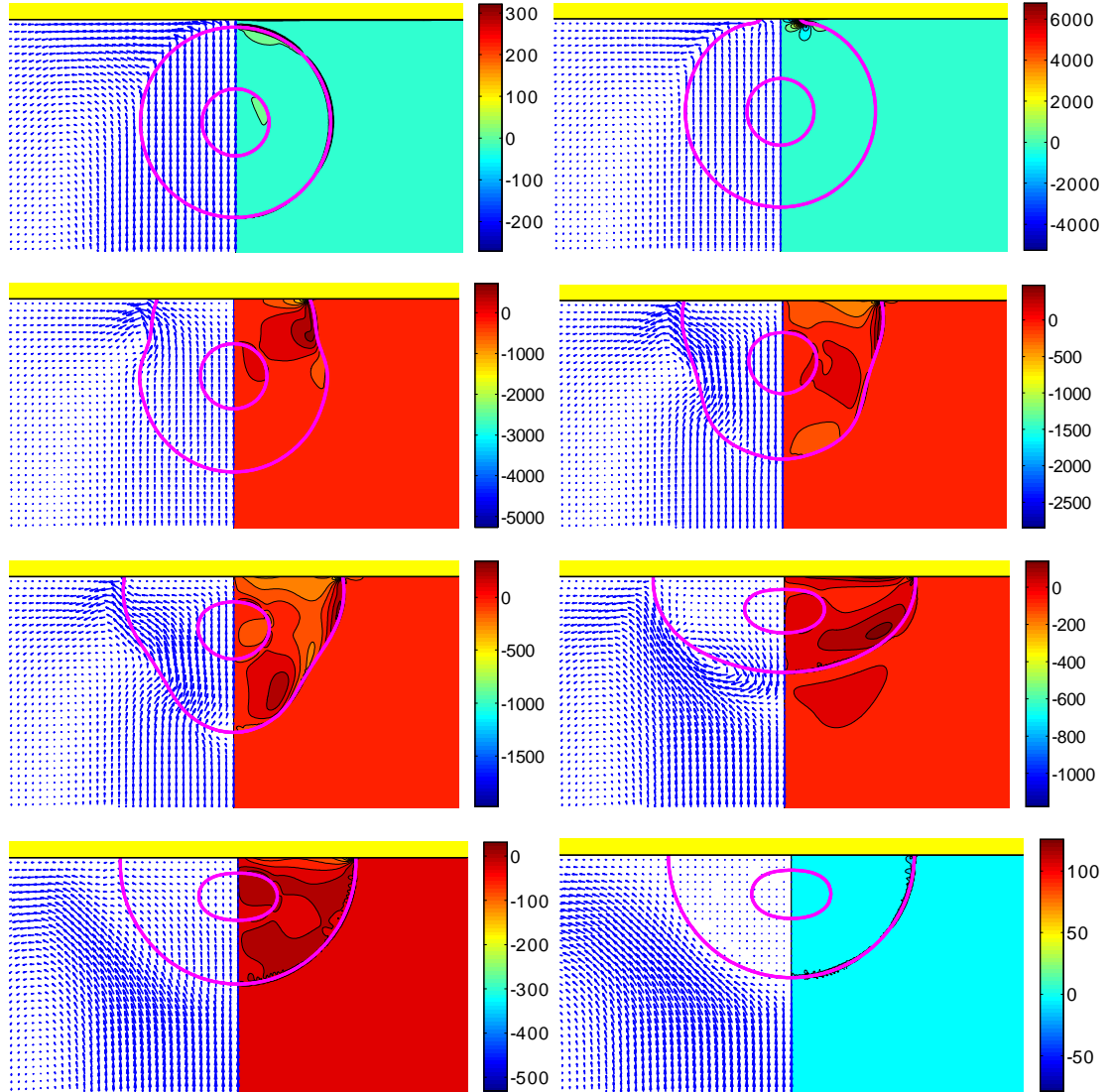


Figure 2.9: Evolution of compound droplet impacting on a flat surface ([left half] velocity vectors and [right half] shear contours). Time evolves from left to right and from top to bottom, and the snapshots are taken at times $t^* = 0.000269, 0.0541, 0.1351, 0.2162, 0.2703, 0.5135, 1.0270$ and 3.8432 . ($We = 0.5, Re = 30, d_o/d_i = 2.85, \sigma_o/\sigma_i = 2541, \mu_c/\mu_d = 10$).

Next, we investigate the consequences of variation of the governing dimensionless parameters. In keeping with our emphasis on the inner droplet, we shall define a gross deformation measure as:

$$D = \frac{W_b - H_b}{W_b + H_b},$$

where W_b and H_b are the maximum droplet dimensions in the radial and axial directions, respectively. Note that, t^{**} (in Figs. 3.8, 3.10, 3.12, 3.14, 3.16, 3.18) is obtained by subtracting the time period between droplet initiation and attachment to the wall from the total elapsed time t , and nondimensionalized again with \mathcal{T} .

The Reynolds number plays a role in the extent of spreading and in the dynamic contact angle, as shown in Fig. 2.10. A relative increase in inertial effects leads to a more powerful collision and subsequent cycling between spread and recoil (see $Re = 45$), although all simulations with different Reynolds number converge to the same equilibrium extent of spread. Slowness in spreading for small Re values can also be observed from the evolution of dynamic contact angle, in Fig. 2.10b. The deformation and rate of deformation of the cell are plotted as a function of dimensionless time for $Re = 15, 20, 30, 40$ and 45 in Fig. 2.11. It is observed that peak cell deformation and rate of deformation increase as Reynolds number increases. Note that cell deformation continues to decrease, even as the cell-encapsulating droplet reaches a steady spread, e.g., at $t^* = 4.0$ for $Re = 30$ in Fig. 3.6. The simulation is stopped around $t^* = 4$ to limit computational expense. Of course, we expect cell deformation to have vanished at steady state.

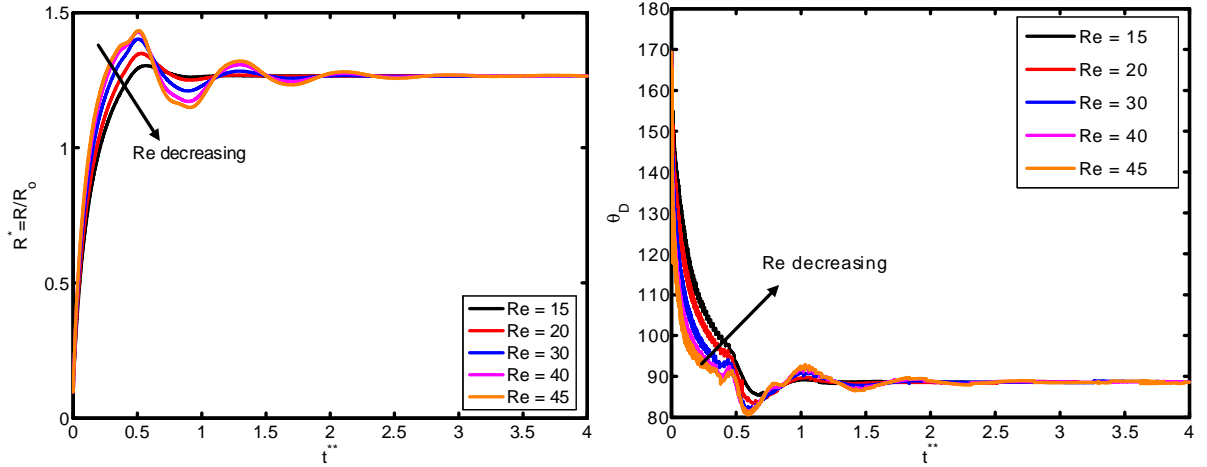


Figure 2.10: (a) Spread factor and (b) dynamic contact angle versus non-dimensional time for $Re = 15, 20, 30, 40$ and 45 . ($We = 0.5$, $d_o/d_i = 2.85$, $\sigma_o/\sigma_i = 2541$, $\mu_c/\mu_d = 10$).

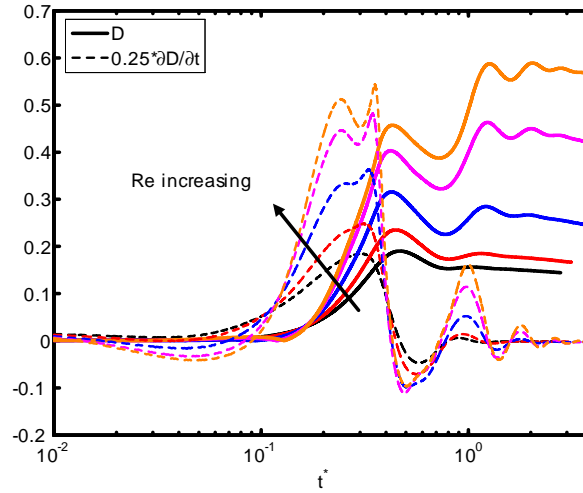


Figure 2.11: Deformation versus non-dimensional time for $Re = 15, 20, 30, 40$ and 45 . ($We = 0.5$, $d_o/d_i = 2.85$, $\sigma_o/\sigma_i = 2541$, $\mu_c/\mu_d = 10$).

Next, we examine the effects of the Weber number by varying the Weber number between 0.25 and 10 while keeping the other parameters fixed as in the base case. The results are plotted in Fig. 2.12 for the extent of spread and the dynamic contact angle. As can be seen from this figure, there is a change in trend around $We = 2$. Maximum spread initially decreases as Weber number increases. Thereafter, it starts to increase with increasing Weber number in a similar way as also observed by Muradoglu and Tasoglu [45] for the

simple droplet spreading in the range $We = 10$ to 1080. Another observation is that the encapsulating droplet reaches equilibrium conditions faster as Weber number decreases. Deformation and rate of deformation of the cell are plotted in Fig. 2.13 as a function of dimensionless time for $We = 0.25, 0.5, 1.0, 2.0, 5.0$ and 10.0. A similar trend is also observed in the deformation: it first decreases with We until $We = 2$, and then it increases with increasing Weber number. On the other hand, the maximum rate of deformation consistently decreases as We increases.

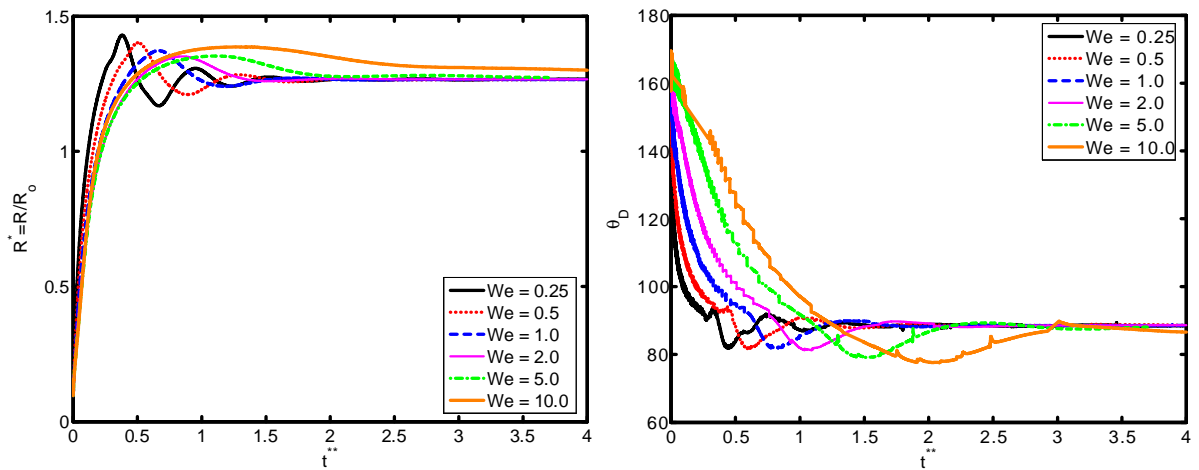


Figure 2.12: (a) Spread factor and (b) dynamic contact angle versus non-dimensional time for $We = 0.25, 0.5, 1.0, 2.0, 5.0$ and 10.0. ($Re = 30, d_o/d_i = 2.85, \sigma_o/\sigma_i = 2541, \mu_c/\mu_d = 10$).

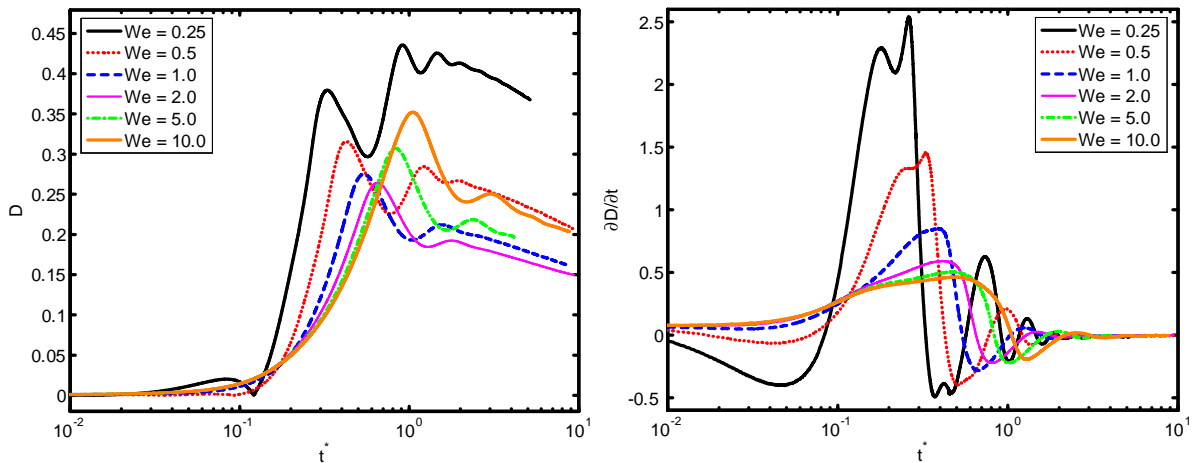


Figure 2.13: (a) Deformation and (b) rate of deformation versus non-dimensional time for $We = 0.25, 0.5, 1.0, 2.0, 5.0$ and 10.0. ($Re = 30, d_o/d_i = 2.85, \sigma_o/\sigma_i = 2541, \mu_c/\mu_d = 10$).

It is desirable that the droplet size is sufficiently small so that it contains only a single cell but it is large enough to provide sufficient protection during the collision. The current printing technologies allow us to control the droplet size precisely within terms of microns. Therefore it is important to examine the effects of the relative droplet size on the viability of the cell. For this purpose, simulations are performed for various values of diameter ratio in the range $d_o/d_i = 1.5$ to 3.5 while keeping the other parameters the same as those in the base case. Figure 2.14 shows the extent of spread and the dynamic contact angle for various values of the diameter ratio as a function of dimensionless time. Although the dynamics look similar for different values of d_o/d_i , an increase in d_o/d_i leads to a slightly stronger spread and recoil. Deformation and rate of deformation of cell are plotted as a function of dimensionless time for $d_o/d_i = 1.5, 2.0, 2.5, 2.85, 3.0$ and 3.5 in Fig. 2.15. It is observed that both deformation and rate of deformation increase as the ratio of encapsulating droplet diameter to cell diameter decreases.

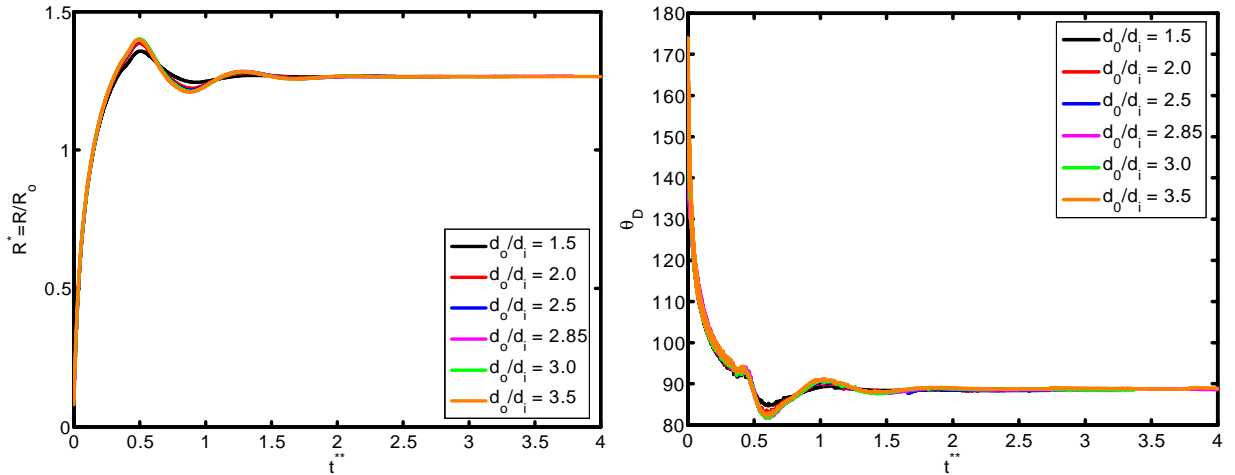


Figure 2.14: (a) Spread factor and (b) dynamic contact angle versus non-dimensional time for $d_o/d_i = 1.5, 2.0, 2.5, 2.85, 3.0$ and 3.5. ($We = 0.5$, $Re = 30$, $\sigma_o/\sigma_i = 2541$, $\mu_c/\mu_d = 10$).

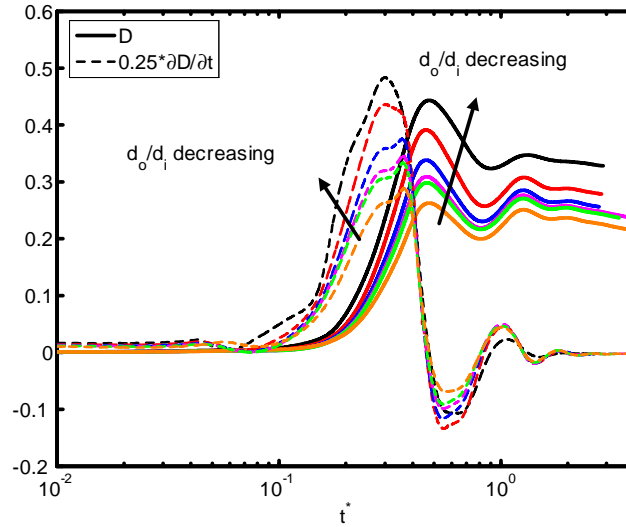


Figure 2.15: Deformation and rate of deformation versus non-dimensional time for $d_o/d_i = 1.5, 2.0, 2.5, 2.85, 3.0$ and 3.5 . ($We = 0.5$, $Re = 30$, $\sigma_o/\sigma_i = 2541$, $\mu_c/\mu_d = 10$).

The surface tension is another important parameter in terms of characterizing dynamics of outer droplet, which may effect cell deformation during the printing process. Simulations are performed for the surface tension ratios $\sigma_o/\sigma_i = 10, 20, 50, 500, 2541$ and 5000 while keeping the other parameters the same as those in the base case to investigate the effects of the surface tension on the cell viability. The time evolutions of the spread factor and the dynamic contact angle are plotted in Fig. 2.16. It is interesting to observe that the ratio of surface tension σ_o/σ_i does not have a significant influence on the spread rate and the dynamic contact angle. The deformation and rate of deformation of cell are also plotted Fig. 2.17 as a function of dimensionless time for $\sigma_o/\sigma_i = 10, 20, 50, 500, 2541$ and 5000 . It is found that cell deformation and rate of deformation increase as the ratio of surface tension at the air-solution interface to that of the solution-cell interface increases. In contrast, the

cell relaxes to its spherical shape faster for smaller values of σ_o/σ_i .

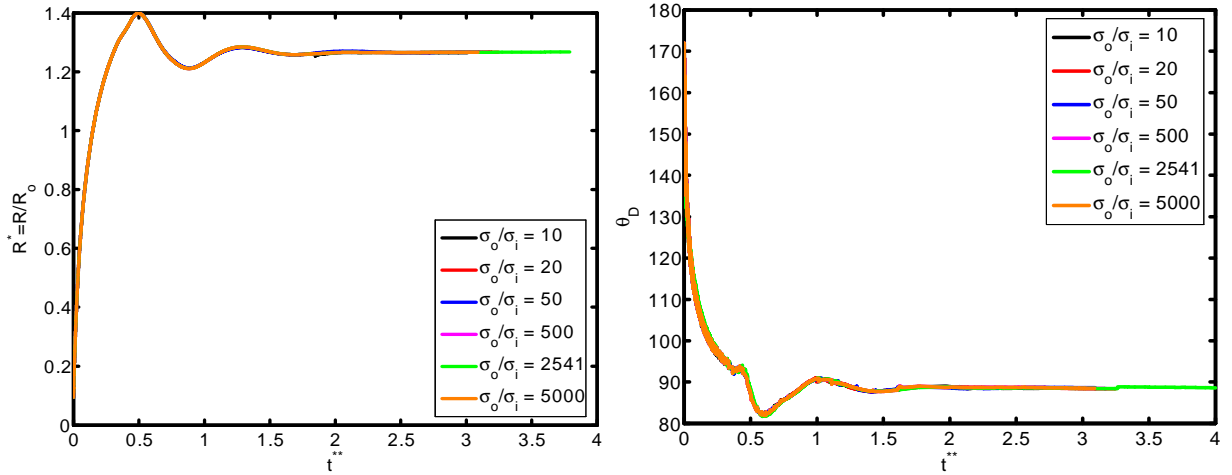


Figure 2.16 (a) Spread factor and (b) dynamic contact angle versus non-dimensional time for $\sigma_o/\sigma_i = 10, 20, 50, 500, 2541$ and 5000 . ($We = 0.5, Re = 30, d_o/d_i = 2.85, \mu_c/\mu_d = 10$).

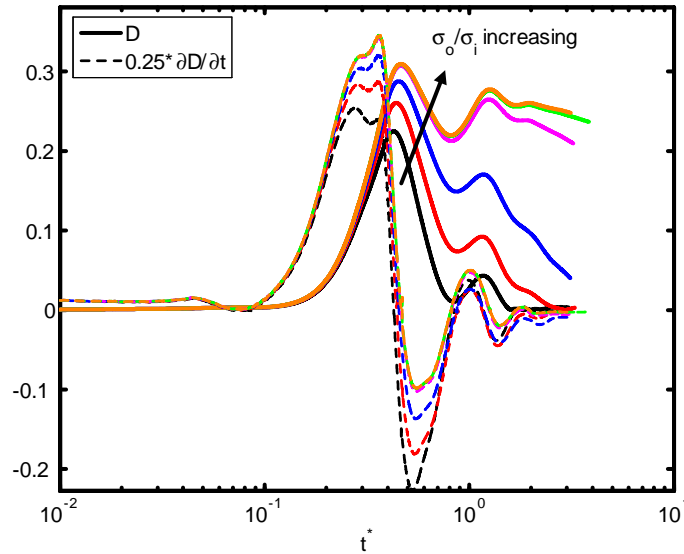


Figure 2.17: Deformation and rate of deformation versus non-dimensional time for $\sigma_o/\sigma_i = 10, 20, 50, 500, 2541$ and 5000 . ($We = 0.5, Re = 30, d_o/d_i = 2.85, \mu_c/\mu_d = 10$)

Current cell printing techniques used in tissue engineering and bio-preservation encapsulate cells in low viscosity solutions such as cell media as well as higher viscosity biomaterials such as collagen and cryoprotectant agents. Therefore, we also investigated the consequences of variation of the viscosity ratio between the cell and the cell-encapsulating droplet for the

range $\mu_c/\mu_d = 2, 5, 10, 20$ and 40 with other parameters constant. In Fig. 2.18, the extent of spread and the dynamic contact angle are plotted as a function of dimensionless time. It is found that the viscosity ratio μ_c/μ_d does not have any significant influence on the spreading rate and the dynamic contact angle. Cell deformation and rate of deformation are also plotted in Fig. 2.19 as a function of dimensionless time for $\mu_c/\mu_d = 2, 5, 10, 20$ and 40 . It is observed that cell deformation and rate of deformation increase as viscosity ratio of cell to that of encapsulating droplet decreases.

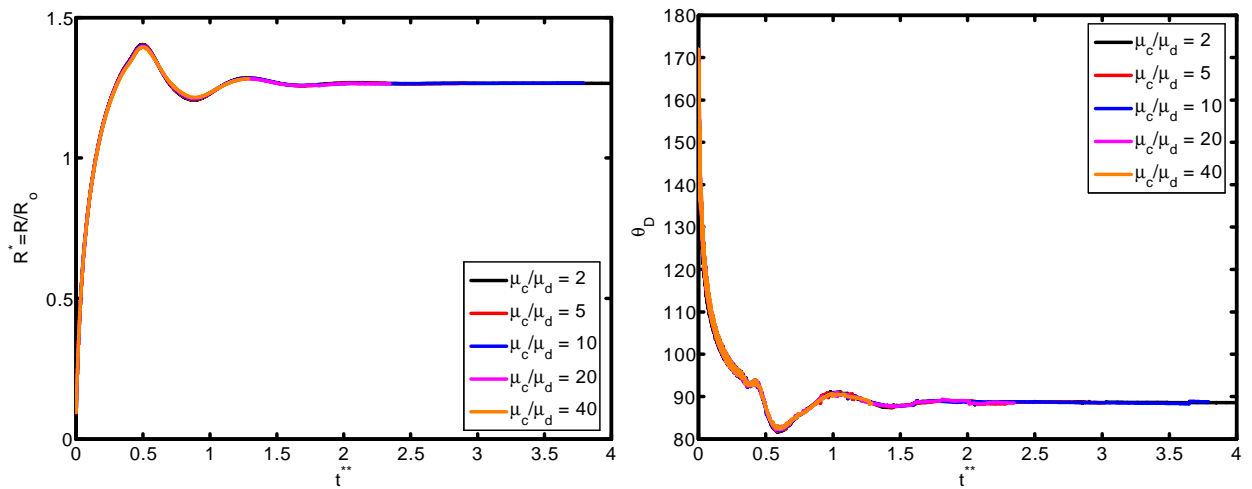


Figure 2.18 (a) Spread factor and (b) dynamic contact angle versus non-dimensional time for $\mu_c/\mu_d = 2, 5, 10, 20$ and 40 . ($We = 0.5$, $Re = 30$, $d_o/d_i = 2.85$, $\sigma_o/\sigma_i = 2541$).

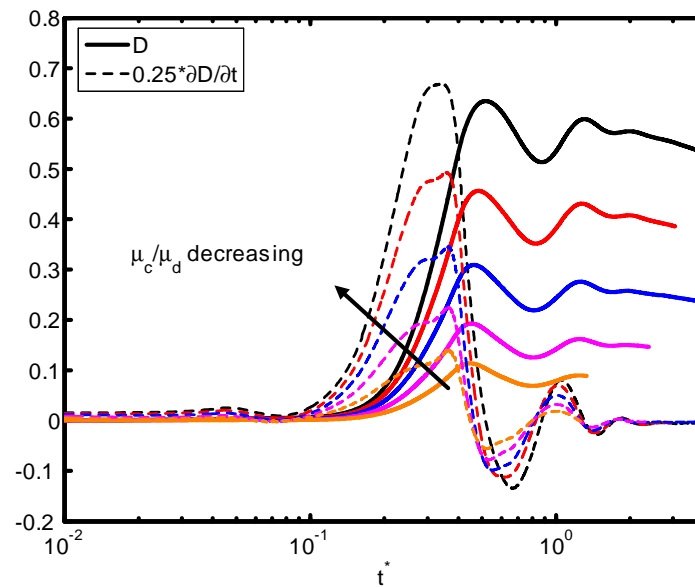


Figure 2.19: Deformation and rate of deformation versus non-dimensional time for $\mu_c/\mu_d = 2, 5, 10, 20$ and 40 . ($We = 0.5, Re = 30, d_o/d_i = 2.85, \sigma_o/\sigma_i = 2541$).

We finally investigate the effects of the equilibrium contact angle. For this purpose, simulations are performed for $\theta_e = 30^\circ, 45^\circ, 60^\circ, 75^\circ, 90^\circ, 105^\circ$, and 120° while the other parameters are kept the same as those in the base case. Note that static contact angle is dependent on the surface tensions of all involved phases according to Young's equation. However, the static contact angle can be changed without changing the surface tension at air-liquid interface by simply using different materials (with different surface energy) for the substrate. The extent of spread and the dynamic contact angle are plotted as a function of dimensionless time in Fig. 2.20. As can be seen, droplets correctly relax to their equilibrium contact angles as the equilibrium conditions are reached. Maximum extent of spread increases as θ_e decreases. In Fig. 2.21, deformation and rate of deformation of cell are plotted as a function of dimensionless time for $\theta_e = 30^\circ, 45^\circ, 60^\circ, 75^\circ, 90^\circ, 105^\circ$, and 120° . It is found that cell deformation and rate of deformation increase as the equilibrium contact angle decreases.

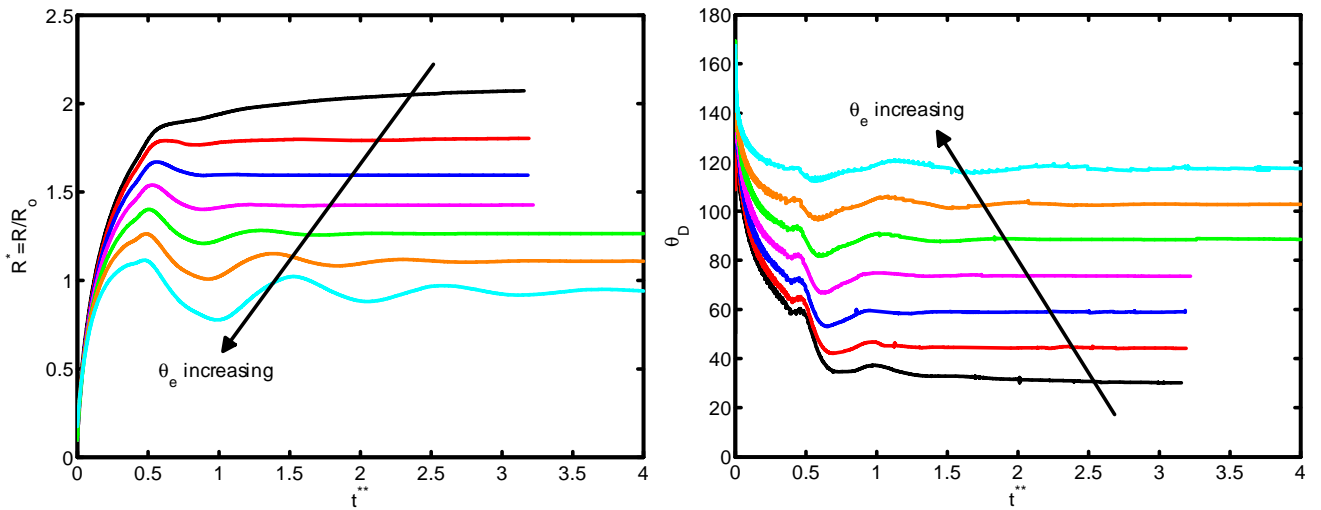


Figure 2.20: (a) Spread factor and (b) dynamic contact angle versus non-dimensional time for $\theta_e = 30^\circ, 45^\circ, 60^\circ, 75^\circ, 90^\circ, 105^\circ$, and 120° . ($We = 0.5, Re = 30, d_o/d_i = 2.85, \sigma_o/\sigma_i = 2541, \mu_c/\mu_d = 10$).

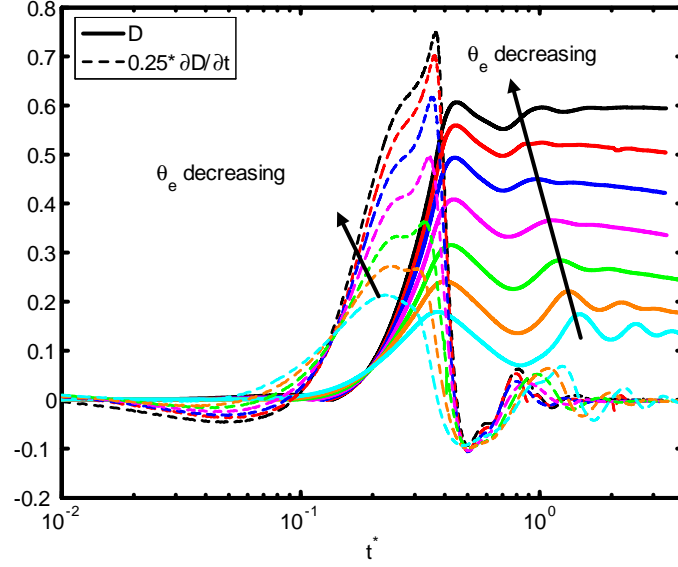


Figure 2.21: Deformation and rate of deformation versus non-dimensional time for $\theta_e = 30^\circ$, 45° , 60° , 75° , 90° , 105° , and 120° . ($We = 0.5$, $Re = 30$, $d_o/d_i = 2.85$, $\sigma_o/\sigma_i = 2541$, $\mu_c/\mu_d = 10$).

Thus far, the effects of governing nondimensional numbers on the deformation and rate of deformation of the cell have been investigated. Now, we attempt to estimate cell viability during the impact and spreading processes by using the method suggested by Takamatsu et al. [47]. This method is based on the experimental data obtained from the compression of cells between parallel plates. The model assumes that cells deform symmetrically during the motion of plates. Because the present simulations consistently indicate that the cells deform quite symmetrically (see for instance, the evolution of cell interface plotted in Fig. 2.22), we use this method to predict the viability of the cell during the printing process. Takamatsu et al. [47] suggest that the viability of an individual cell (η) is given by

$$\eta(\gamma) = \begin{cases} 1 & \text{for } \gamma < \gamma_{cr} - \Delta\gamma, \\ \frac{1}{2} - \frac{\gamma - \gamma_{cr}}{2\Delta\gamma} & \text{for } \gamma_{cr} - \Delta\gamma \leq \gamma \leq \gamma_{cr} + \Delta\gamma, \\ 0 & \text{for } \gamma > \gamma_{cr} + \Delta\gamma, \end{cases} \quad (2.9)$$

where $\gamma = A/A_o$ with A and A_o being the surface areas of the deformed and undeformed cells, respectively. Based on the curve fit to the experimental data, the other parameters in Eq. (2.9) are specified as $\gamma_{cr} = 1.5$ and $\Delta\gamma = 0.4$. The viability of the cells based on the

present simulations are summarized in Table 2.3. Note that only one parameter is varied in each row of Table 2.3 while all others are set the values in the base case. As can be seen in this table, the cell viability rapidly decreases as θ_e and μ_c/μ_d decrease. Cell viabilities are near or exceed 90% for the ranges of Re , We , d_o/d_i and σ_o/σ_i that we studied here. Note that although the minimum static contact angle that we studied (30°) is still larger than the value in the experimental study (10°), viability is decreased to an unacceptable small value, i.e. 26%. However, as we mentioned before, μ_c/μ_d is set to 10 in varying θ_e case and in other cases except the case in which μ_c/μ_d is varied. Given the fact that cell viscosity is much higher than that of ambient fluid [34, 35, 36, 37] and higher μ_c/μ_d leads to higher viability, a simple question arises: what is the combined effect of higher μ_c/μ_d and lower θ_e on viability? In this study, further computations are not performed because required computational time is not reasonable with the present method. However, this study provides initial insight of viability trends with respect to several governing nondimensional numbers.

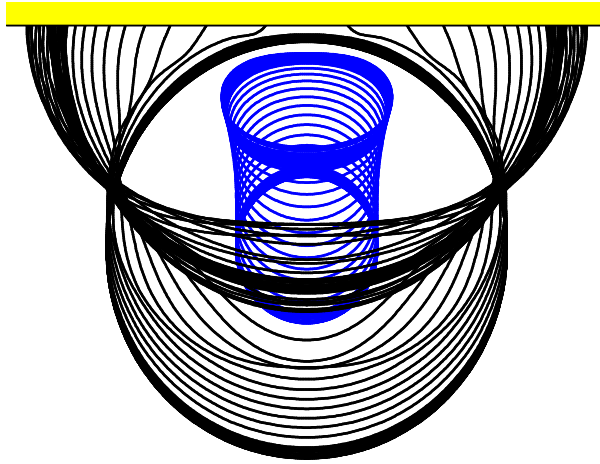


Figure 2.22: Evolution of compound droplet. ($We = 0.5$, $Re = 30$, $d_o/d_i = 2.85$, $\sigma_o/\sigma_i = 2541$, $\mu_c/\mu_d = 10$).

Table 2.3: Viabilities of cells

Re	15	20	30	40	45		
η	100.00	100.00	100.00	90.38	86.31		
We	0.25	0.5	1	2	5	10	
η	88.62	100.00	100.00	100.00	100.00	98.67	
d_o/d_i	1.5	2.0	2.5	2.85	3.0	3.5	
η	88.05	92.97	97.90	100.00	100.00	100.00	
σ_o/σ_i	10	20	50	500	2541	5000	
η	100.00	100.00	100.00	100.00	100.00	100.00	
μ_c/μ_d	2	5	10	20	40		
η	44.07	88.43	100.00	100.00	100.00		
θ_e	30°	45°	60°	75°	90°	105°	120°
η	26.15	54.81	80.77	91.84	100.00	100.00	100.00

Chapter 3

CONCLUSIONS

Impact and spreading of a compound droplet on a smooth flat surface are studied computationally using a finite-difference/front-tracking method in an axisymmetric setting. The compound droplet is proposed as a model for printing of droplet-encapsulated biological cells [17, 18]. The cell is modeled as a highly viscous Newtonian droplet that is encapsulated by a less viscous Newtonian liquid. It is hypothesized that the cell viability is mainly dependent on the cell deformation and its rate. Therefore the model is used to investigate the optimal conditions that yield minimum deformation and deformation rate. The experimental conditions of Demirci and Montesano [18] are taken as the base case and then the effects of nondimensional parameters on the cell viability are investigated by varying each parameter at a time systematically while keeping the others the same as those in the base case.

Since the numerical method has been already validated comprehensively for a simple droplet impact and spreading on a flat surface, validation tests are performed here to assess the performance of the method for compound droplet. For this purpose, it is first shown that the compound droplet correctly relaxes to its equilibrium shape when it impacts and spreads on a flat surface for a wide range of Eötvös numbers. Then the treatment of the contact line is validated against the experimental data for a simple glycerin droplet spreading on a wax substrate. Finally, the numerical method is applied to simulate the buoyancy-driven motion and deformation of compound droplet, and results are found to be in a good agreement with the experimental data of Mori [49] and also with the finite element simulations of Bazhlekova et al. [31].

After validating the numerical method, computations are performed to examine the effects of the relevant dimensionless parameters on the dynamics of compound droplet impact and spreading on a flat surface. It is found that maximum spreading of the cell-encapsulating droplet increases as the Reynolds number (Re) increases. As Weber number (We) increases,

maximum spread first decreases until $We = 2$, then it increases. The diameter ratio, the viscosity of the cell and the surface tension at the solution-cell interface are found to have no significant influence on the spreading of the encapsulating droplet in the range we studied here. It is found that the maximum spreading and the equilibrium extent of spread increase as the equilibrium contact angle decreases as expected. Deformation and rate of deformation of the cell (inner droplet) increase as Reynolds number and surface tension ratio of the air-solution interface to the solution-cell interface (σ_o/σ_i) increase. For smaller σ_o/σ_i , the cell relaxes to its equilibrium shape faster. Deformation and rate of deformation of the cell increases as diameter ratio of encapsulating droplet to cell (d_o/d_i) and viscosity ratio of cell to encapsulating droplet (μ_c/μ_d) decreases. It is observed that there is a change in the trend of the peak deformation for different Weber numbers. Maximum deformation first decreases until $We = 2$, then it increases with increasing Weber number. On the other hand, the peak rate of deformation consistently decreases as We increases. Finally, we employ a relation to fit to experimental data of compression of cells between two parallel plates [47] to estimate the effects of cell deformation on viability. It is found that the cell viability rapidly decreases as θ_e and μ_c/μ_d decrease. Cell viability is near or over 90% for the ranges of Re , We , d_o/d_i and σ_o/σ_i that we studied in this paper. The cell viability is found to decrease rapidly as the equilibrium contact angle decreases below 60° . This can be partly attributed to low viscosity ratio ($\mu_c/\mu_d = 10$) in varying θ_e case.

The goal of this work was to develop a framework for investigating relative importance of governing nondimensional numbers: Re , We , d_o/d_i , σ_o/σ_i , μ_c/μ_d , and θ_e on cell viability for the problem of deposition of cell encapsulating droplets. The analysis pointed out along the way that a number of parameters such as μ_c/μ_d and θ_e should be perturbed simultaneously.

In Appendix A, Oldroyd-B fluid model is used for the inner droplet in order to represent memory or history effects and viscoelastic nature of the biological cells. The constitutive equations for the Oldroyd-B fluid model are solved together with the mass and momentum conservation equations in axisymmetric frame using the front-tracking/finite-difference method. An implicit method is used for the integration of the evolution equations of total stress tensor in Oldroyd-B model and factorization approximation is used to accelerate the solution at each time step. A few sample results are presented to show the consistency of Oldroyd-B fluid model with the corresponding Newtonian fluid model.

Appendix A

NON-NEWTONIAN FLUID MODEL

The biological cells are extremely complex and Newtonian models are not sufficient to represent their complex structure. The main deficiency of the Newtonian fluid model is that it does not have any “memory”, i.e., the shear stresses acting on the Newtonian fluid are determined by the local rate of strain tensor. On the other hand, the biological cells are known to have a strong memory and exhibit a viscoelastic like behavior. Therefore a good model must be able to reflect the memory or history effects and viscoelastic behavior of the biological cells. There are various types of non-Newtonian fluid models that attempt to model the viscoelastic behavior of fluids including FENE-CR, Oldroyd-B, Maxwell and Boger fluids that have been widely used in the literature [52, 53, 54, 55, 56, 57, 58]. Some of these existing models contain up to eight independent parameters mainly related to the chemical structure and viscoelasticity of the polymers. In this study, the Oldroyd-B fluid is used to model the biological cell since it involves only two extra parameters, i.e., relaxation time and polymeric viscosity, and it has been widely used as a model for various types of biological cells. For instance, Zhou et al. [59] simulated transport of Neutrophil through capillaries using Oldroyd-B model and investigated effects of viscoelasticity in the process.

The motion and deformation of a single Oldroyd-B drop have been widely studied in the literature. Toose et al. [57] employed a boundary-integral method to investigate the effects of viscoelasticity on drop dynamics. Yue et al. [56] used a level-set method and studied the viscoelastic effects on drop dynamics in simple shear flows. Ramaswamy and Leal [55] modeled the drop deformation in uniaxial flow and Hooper et al. [53] employed an implicit integration scheme to track drop motion in axisymmetric coordinates. Viscoelastic drop/Newtonian matrix system was also modeled in three dimensions by Khismatullin et al. [54] using the VOF-PROST algorithm. Aggarwal and Sarkar [58] employed a three dimensional finite-difference/front-tracking method to investigate the deformation of an Oldroyd-B or Newtonian drop in a viscoelastic fluid and concluded that the front-tracking

is an effective method to solve the constitutive equations of the Oldroyd-B fluid in the context of interfacial flows. The previous studies generally dealt with deformation of a single non-Newtonian droplet in a simple shear or axisymmetric flow. To the best of our knowledge, only Toose et al. [60] modeled compound drop deformation under uniaxial flow. However, none of these studies investigated the impact and spreading of a viscoelastic compound droplet on a substrate.

In this study, we aim to investigate the impact and spreading of a compound droplet with the inner droplet being an Oldroyd -B fluid on a flat surface as a model for the single cell epitaxy. In particular, focus is placed on the deformation and rate of deformation of the inner droplet during impingement of the compound droplet. The constitutive equations are again solved in the entire computational domain using the front-tracking/finite-difference method [43].

The Oldroyd-B Fluid Model

First, the constitutive equations are briefly discussed in this section. The incompressible mass and momentum equations can be written as [52]

$$\nabla \cdot \mathbf{u} = 0, \quad (\text{A.1})$$

$$\rho \left(\frac{\partial \mathbf{u}}{\partial t} + \mathbf{u} \cdot \nabla \mathbf{u} \right) = \nabla \cdot \boldsymbol{\tau} + \mathbf{F}, \quad (\text{A.2})$$

where, $\boldsymbol{\tau}$ is the total stress tensor given by

$$\boldsymbol{\tau} = -p\mathbf{I} + \mathbf{T} + \mu_s \mathbf{S}, \quad (\text{A.3})$$

where p is the pressure, \mathbf{T} is the extra stress tensor, μ_s is the solvent viscosity and $\mathbf{S} = \nabla \mathbf{u} + \nabla \mathbf{u}^T$ is the rate of strain tensor. The last term in the momentum equation is the body forces composed of the gravitational and surface tension forces. In the single cell epitaxy, the gravitational forces are usually negligible compared to the other effects. Therefore the body force term \mathbf{F} includes only surface tension forces and is given by

$$\mathbf{F} = \int_A \sigma \kappa \mathbf{n} \delta(x - x_f), \quad (\text{A.4})$$

where σ is the surface tension, κ is twice the curvature, and \mathbf{n} is unit vector normal to the interface. The surface tension only acts on the interface as indicated by delta function δ ,

whose arguments x and x_f are the point at which the equation is evaluated and the point at the interface, respectively.

For an Oldroyd-B fluid, the extra stress tensor \mathbf{T} evolves by

$$\lambda \tilde{\mathbf{T}} + \mathbf{T} = \mu_p \mathbf{S}, \quad (\text{A.5})$$

where λ is the relaxation time, μ_p is the polymeric viscosity and $\tilde{\mathbf{T}}$ is the upper convected time derivative defined as

$$\tilde{\mathbf{T}} = \frac{\partial \mathbf{T}}{\partial t} + (\mathbf{u} \cdot \nabla) \mathbf{T} - (\nabla \mathbf{u}) \mathbf{T} - \mathbf{T} (\nabla \mathbf{u})^T. \quad (\text{A.6})$$

The material properties density (ρ), polymeric viscosity (μ_p), solvent viscosity (μ_s) and the relaxation time (λ) are smoothed using the indicator function as

$$\begin{aligned} \rho &= \begin{cases} \rho_d I(r, z, t) + \rho_o (1 - I(r, z, t)) & \text{If } I(r, z, t) \leq 1.0 \\ \rho_c (I(r, z, t) - 1) + \rho_d (2 - I(r, z, t)) & \text{Otherwise,} \end{cases} \\ \mu_p &= \begin{cases} \mu_{pd} I(r, z, t) + \mu_{po} (1 - I(r, z, t)) & \text{If } I(r, z, t) \leq 1.0 \\ \mu_{po} (I(r, z, t) - 1) + \mu_{pd} (2 - I(r, z, t)) & \text{Otherwise,} \end{cases} \\ \mu_s &= \begin{cases} \mu_{sd} I(r, z, t) + \mu_{so} (1 - I(r, z, t)) & \text{If } I(r, z, t) \leq 1.0 \\ \mu_{so} (I(r, z, t) - 1) + \mu_{sd} (2 - I(r, z, t)) & \text{Otherwise,} \end{cases} \\ \lambda &= \begin{cases} \lambda_d I(r, z, t) + \lambda_o (1 - I(r, z, t)) & \text{If } I(r, z, t) \leq 1.0 \\ \lambda_c (I(r, z, t) - 1) + \lambda_d (2 - I(r, z, t)) & \text{Otherwise,} \end{cases} \end{aligned} \quad (\text{A.7})$$

where the subscripts “c”, “d” and “o” denote properties of the inner droplet, encapsulating droplet and the ambient fluid, respectively.

Numerical Method

The projection method is used to integrate the flow equations. The semi-discretized equations are first written as

$$\frac{\rho^{n+1} \mathbf{u}^{n+1} - \rho^n \mathbf{u}^n}{\Delta t} = -\nabla p^{n+1} - \nabla \cdot (\rho \mathbf{u} \mathbf{u})^n + (\nabla \cdot \mathbf{T})^n + \mu_s (\nabla \cdot \mathbf{S})^n + \mathbf{F}^n, \quad (\text{A.8})$$

$$\nabla \cdot \mathbf{u}^n = \nabla \cdot \mathbf{u}^{n+1} = 0. \quad (\text{A.9})$$

Then, the momentum equation is decomposed as

$$\frac{\rho^{n+1}\mathbf{u}^* - \rho^n\mathbf{u}^n}{\Delta t} = -\nabla \cdot (\rho\mathbf{u}\mathbf{u})^n + (\nabla \cdot \mathbf{T})^n + \mu_s(\nabla \cdot \mathbf{S})^n + \mathbf{F}^n, \quad (\text{A.10})$$

$$\frac{\rho^{n+1}\mathbf{u}^{n+1} - \rho^{n+1}\mathbf{u}^*}{\Delta t} = -\nabla p^{n+1}, \quad (\text{A.11})$$

where \mathbf{u}^* represents the unprojected velocity field. The spatial derivatives are approximated using central differences on a staggered grid as was done for the Newtonian case. Taking divergence of Eq. A.11 and using the incompressibility condition results in the Poisson equation for the pressure field

$$\nabla \cdot \left(\frac{\nabla p}{\rho^{n+1}} \right) = \frac{1}{\Delta t} \nabla \cdot \mathbf{u}^*, \quad (\text{A.12})$$

which is solved using a multigrid method as done in the Newtonian case. Then the projected or corrected velocity field is computed as

$$\mathbf{u}^{n+1} = \mathbf{u}^* - \frac{\Delta t}{\rho^{n+1}} \nabla p^{n+1}. \quad (\text{A.13})$$

The constitutive equation for the extra stress term Eq. A.5 is solved using a semi implicit time integration scheme. Assuming that the flow is axisymmetric, Eq. A.5 is discretized as,

$$\lambda \left(\frac{\mathbf{T}^{n+1} - \mathbf{T}^n}{\Delta t} + (u_r^n \frac{\partial}{\partial r} + u_z^n \frac{\partial}{\partial z}) \mathbf{T}^{n+1} \right) + \mathbf{T}^{n+1} = A_3, \quad (\text{A.14})$$

where

$$A_3 = \lambda [(\nabla\mathbf{u})\mathbf{T} + \mathbf{T}(\nabla\mathbf{u}^T)]^n + \mu_p\mathbf{S}^n + \lambda\mathbf{T}^n, \quad (\text{A.15})$$

which requires inversion of a large sparse matrix. In order to reduce computational cost, Eq. A.14 is factorized as

$$(\lambda + \Delta t) \left(I + \frac{\lambda}{\lambda + \Delta t} u_r^n \Delta t \frac{\partial}{\partial r} \right) \left(I + \frac{\lambda}{\lambda + \Delta t} u_z^n \Delta t \frac{\partial}{\partial z} \right) \mathbf{T}^{n+1} = A_3, \quad (\text{A.16})$$

which can be solved very efficiently in two steps. In each step, a tri-diagonal system is solved using the Thomas algorithm [61]. The components of the A_3 corresponding to T_{11}, T_{22} and T_{12} are as follows,

$$\begin{aligned}
A_{311} &= \Delta t \left(2\lambda \left[T_{11} \frac{\partial u_r}{\partial r} + T_{12} \frac{\partial u_z}{\partial r} \right] + 2\mu_p \frac{\partial u_r}{\partial r} \right) + \lambda T_{11} \\
A_{322} &= \Delta t \left(2\lambda \left[T_{12} \frac{\partial u_r}{\partial z} + T_{22} \frac{\partial u_z}{\partial z} \right] + 2\mu_p \frac{\partial u_z}{\partial z} \right) + \lambda T_{22} \\
A_{312} &= A_{321} = \Delta t \left(\lambda \left[T_{12} \left(\frac{\partial u_r}{\partial r} + \frac{\partial u_z}{\partial z} \right) + T_{11} \frac{\partial u_r}{\partial z} + T_{22} \frac{\partial u_z}{\partial r} \right] + \mu_p \left(\frac{\partial u_r}{\partial z} + \frac{\partial u_z}{\partial r} \right) \right) + \lambda T_{12}
\end{aligned}$$

The contact line is treated as described in Chapter 2 for the Newtonian case.

Preliminary Results

The numerical method has been implemented but not tested completely. Here a few results are presented to show the consistency of the Oldroyd-B model with the corresponding Newtonian model. For this purpose, the relaxation time and polymeric viscosity are set to zero while the solvent viscosity is set to the viscosity in the Newtonian fluid. The material properties of the phases are the same as shown in Table 1. The diameter of the encapsulating droplet (d_o) and diameter of the cell (d_i) are again set to $37\mu m$ and $13\mu m$ ($d_o/d_i = 2.85$). The computational domain extends 6 drop radii in the radial direction and 3 drop radii in the axial direction. Surface tension at the air-solution interface and the solution-cell interface are 0.07622 and 0.00003 N/m , respectively ($\sigma_o/\sigma_i = 2541$). The governing dimensionless numbers are, $We = 0.5$, $Re = 30$, $d_o/d_i = 2.85$, $\sigma_o/\sigma_i = 2541$, $\mu_c/\mu_d = 10$, and $\theta_e = 90^\circ$.

Snapshots in Fig. A.1 show the Newtonian and Oldroyd-B solutions at times $t^* = 0.0670$, 0.2690 , 0.6725 and 1.3450 . The computations are performed using a 256×130 grid resolution. Solutions of two methods indicate that deformation on outer and inner drops show good agreement as $\lambda = 0$ and $\mu_p = 0$ for all three phases.

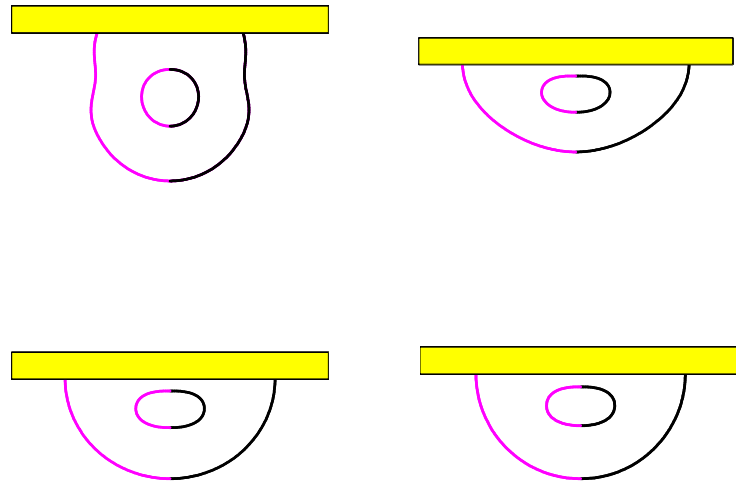


Figure A.1: Comparison of Oldroyd-B and Newtonian Codes for the Newtonian Case at $t^* = 0.0670, 0.2690, 0.6725$ and 1.3450 . (Time evolves from left to right and from top to bottom) (Left side of the plot represents solution with Oldroyd-B code, right side represents Newtonian solution)

In Fig. A.2 the contact angle is plotted against the dimensionless time. This figure clearly shows the consistency between the Newtonian and non-Newtonian models in the Newtonian limit.

The spread factor computed using the Newtonian and non-Newtonian models in the Newtonian limit is plotted in Fig A.3. This figure also confirms the consistency.

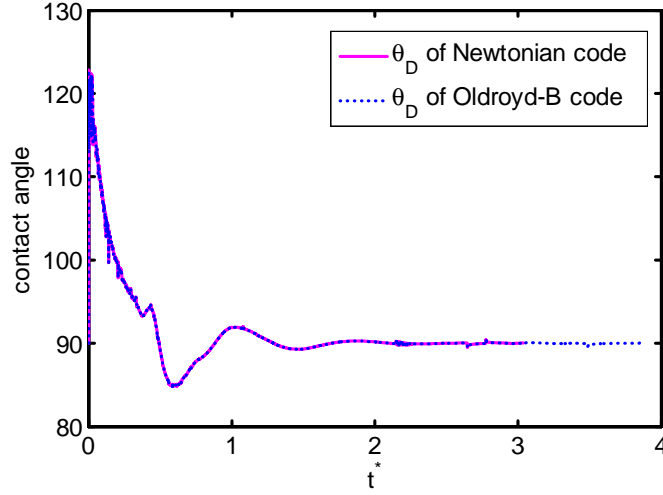


Figure A.2: Contact angle versus time for $We = 0.5$, $Re = 30$, $d_o/d_i = 2.85$, $\sigma_o/\sigma_i = 2541$, $\mu_c/\mu_d = 10$, and $\theta_e = 90^\circ$

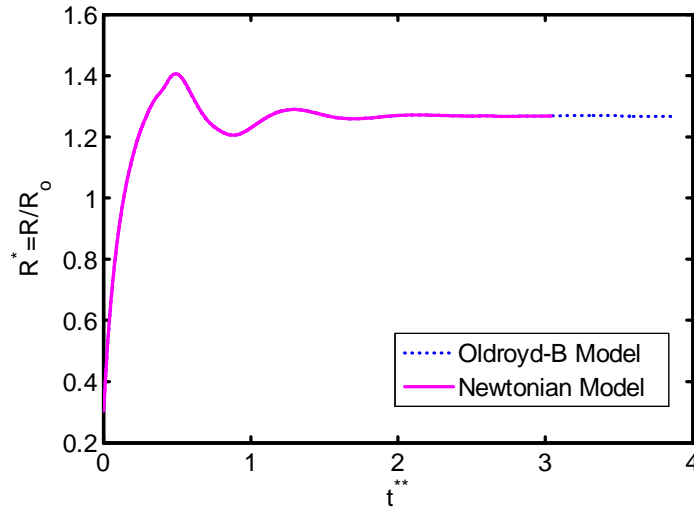


Figure A.3: Spread factor vs time for $We = 0.5$, $Re = 30$, $d_o/d_i = 2.85$, $\sigma_o/\sigma_i = 2541$, $\mu_c/\mu_d = 10$, and $\theta_e = 90^\circ$

Finally, deformation on inner droplet is plotted in Fig A.4. The Oldroyd-B and Newtonian solutions collapse on the same curve showing the consistency.

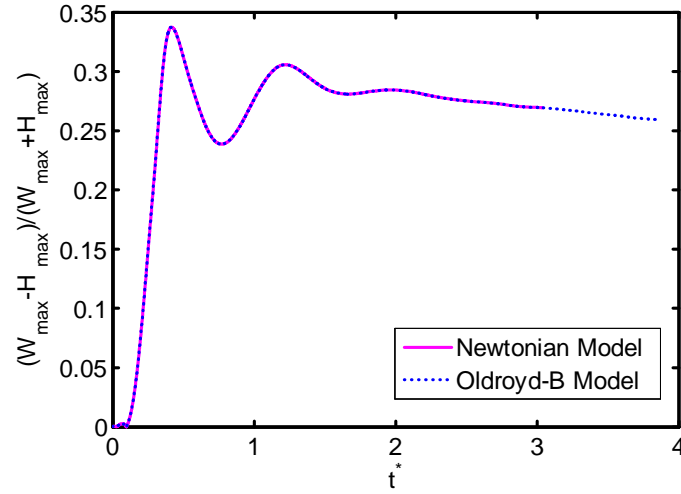


Figure A.4. Deformation vs time for $We = 0.5$, $Re = 30$, $d_o/d_i = 2.85$, $\sigma_o/\sigma_i = 2541$, $\mu_c/\mu_d = 10$, and $\theta_e = 90^\circ$

BIBLIOGRAPHY

- [1] A.L. Yarin, "Drop impact dynamics: Splashing, spreading, receding, bouncing...", *Annu. Rev. Fluid Mech.*, **38**, 159-192 (2006).
- [2] V.E.B. Dussan and S.H. Davis, "On the motion of a fluid-fluid interface along a surface", *J. Fluid Mech.* **65**, 71-95, (1974).
- [3] Y.D. Shikhmurzaev, "Moving contact lines in liquid-liquid-solid systems", *J. Fluid Mech.* **334**, 211-249, (1997).
- [4] J. Fukai, Y. Shiiba, T. Yamamoto, O. Miyatake, D. Poulikakos, C.M. Megaridis and Z. Zhao, "Wetting effects on the spreading of a liquid droplet colliding with a flat surface: experiment and modeling", *Physics of Fluids*, **7**, 236 (1995).
- [5] I.V. Roisman, R. Rioboo and C. Tropea, "Normal impact of a liquid drop on a dry surface: Model for spreading and receding", *Proc. R. Soc. London*, **458**, 1411 (2002).
- [6] M. Bussmann, J. Mostaghimi and S. Chandra, "On a three-dimensional volume tracking model of droplet impact", *Phys. Fluids*, **11**, 1406, (1999).
- [7] S. Manservigi and R. Scardovelli, "A variational approach to the contact angle dynamics of spreading droplets", *Computers & Fluids*, **38(2)**, 406-424 (2008).
- [8] M. Renardy, Y. Renardy and J. Li, "Numerical simulation of moving contact line problem using a volume-of-fluid method", *J. Comput. Phys.* **171**, 243-263, (2001).
- [9] M. Pasandideh-Fard, Y.M. Qiao, S. Chandra and J. Mostaghimi, "Capillary effects during droplet impact on a solid surface", *Physics of Fluids*, **8**, 650 (1996).
- [10] P.D.M. Spelt, "A level-set approach for simulations of flows with multiple moving contact lines with hysteresis", *J. Comput. Phys.*, **207**, 389-404, (2005).

-
- [11] S. Chandra and C.T. Avedisian, "On the collision of a droplet with a solid surface", *Proc. Royal Soc. London Series A-Math. Phys. Eng. Sci.* **432**, 13-41, (1993).
- [12] S. Sikalo, H.D. Wilhelm, I.V. Roisman, S. Jakirlic and C. Tropea, "Dynamic contact angle of spreading droplets: Experiments and simulations", *Physics of Fluids*, **17**, 062103 (2005).
- [13] T. Mao, D.C.S. Kuhn and H. Tran, "Spread and rebound of liquid droplets upon impact on flat surfaces", *AIChE Journal*, **43**, 2169 (1997).
- [14] A.S. Utada, E. Lorenceau, D.R. Link, P.D. Kaplan, H.A. Stone, D.A. Weitz, "Monodisperse double emulsions generated from a microcapillary device", *Science*, **308(5721)**, 537-541 (2005).
- [15] R.H. Chen, S.L. Chiu, T.H. Lin, "Resident time of a compound drop impinging on a hot surface", *Applied Thermal Engineering*, **27(11-12)**, 2079-2085 (2007).
- [16] H. Shintaku, T. Kuwabara, S. Kawano, T. Suzuki, I. Kanno, H. Kotera, "Micro cell encapsulation and its hydrogel-beads production using microfluidic device", *Microsys. Technol.*, **13(8-10)**, 951-958 (2007).
- [17] M. Nakamura, A. Kobayashi, F. Takagi, A. Watanabe, Y. Hiruma, K. Ohuchi, Y. Iwasaki, M. Horie and S. Takatani, "Biocompatible inkjet printing technique for designed seeding of individual cells", *Tissue Engineering*, **11 (11-12)**, 1658-1666, (2005).
- [18] U. Demirci and G. Montesano, "Single Cell Epitaxy by Acoustic Picoliter Droplets", *Lab on a Chip*, **7**, 1139-1145 (2007).
- [19] S. Moon, S.K. Hasan, Y.S. Song, H.O. Keles, F. Manzur, S. Mikkilineni, J.W. Hong, J. Nagatomi, E. Haeggstrom, A. Khademhosseini, and U. Demirci, "Layer by layer 3D tissue epitaxy by cell laden hydrogel droplets", *Tissue Engineering C*, **16(1)**, 157-166 (2010).

-
- [20] T. Boland, X. Tao, B.J. Damon, B. Manley, P. Kesari, S. Jalota, and S. Bhaduri, "Drop-on-demand printing of cells and materials for designer tissue constructs", *Material Science and Engineering*, **27**, 372-376 (2007).
- [21] V. Mironov, T. Boland, T. Trusk, G. Forgacs, and R.R. Markwald, "Organ printing: computer aided jet-based 3D tissue engineering", *TRENDS in Biotechnology*, **21**, 4 (2003).
- [22] U. Demirci and G. Montesano, "Cell encapsulating droplet vitrification", *Lab Chip*, **7**, 1428 - 1433 (2007).
- [23] Y. Song, A. Adler, A. Kayaalp, A. Nureddin, R. Anchan, R. Maas, and U. Demirci, "Vitrification and levitation of a liquid droplet on liquid nitrogen", *PNAS*, doi: 10.1073/pnas.0914059107 (2010).
- [24] R.E. Johnson and S.S. Sadhal, "Fluid mechanics of compound multiphase drops and bubbles", *Annu. Rev. Fluid Mech.*, **17**, 289-320, (1984).
- [25] K.A. Smith, J.M. Ottino and M. Olvera de la Cruz, "Encapsulated drop breakup in shear flow", *Phys. Rev. Lett.*, **93**, 204501, (2004).
- [26] R.H. Engel, S.J. Riggi and M.J. Fahrenbach, "Insulin: Intestinal absorption as water-in-oil-in-water emulsions", *Nature*, **219**, 856-857, (1968).
- [27] R. Langer, "Drug delivery and targeting", *Nature*, **392(6679)**, 5-10, (1998).
- [28] E. Dickinson, J. Evison, J.W. Gramshaw and D. Schwope, "Flavor release from a protein-stabilized water-in-oil-in-water emulsion", *Food Hydrocolloids*, **8(1)**, 63-67, (1994).
- [29] R. Pal, "Rheology of double emulsions", *J. Coll. Interface Sci.*, **307**, 509-515, (2006).
- [30] H.A. Stone and L.G. Leal, "Breakup of concentric double emulsion droplets in linear flows", *J. Fluid Mech.*, **211**, 123-156, (1990).

-
- [31] I.B. Bazhlekov, P.J. Shopov and Z.D. Zapryanov, "Unsteady motion of type-A compound multiphase drop at moderate Reynolds numbers", *J. Colloid Interface Sci.*, **169**, 1-12, (1995).
- [32] S. Kawano, A. Shirai and S. Nagasaka, "Deformations of thin liquid spherical shells in liquid-liquid-gas systems", *Phys. Fluids*, **19** (1), 012105, (2007).
- [33] C. Zhou, O. Yue and J. Feng, "Formation of simple and compound drops in microfluidic devices", *Phys. Fluids*, **18**, 092105, (2006).
- [34] A. Yeung and E. Evans, "Cortical shell-liquid core model for passive flow of liquid-like spherical cells into micropipets", *Biophys. J.*, **56**, 139-149, (1989).
- [35] D. Needham and R.M. Hochmuth, "Rapid flow of passive neutrophils into 4 μm pipet and measurement of cytoplasmic viscosity", *ASME J. Biomech. Eng.*, **112**, 269-278, (1990).
- [36] R. Tran-Son-Tay, D. Needham, A. Yeung and R.M. Hochmuth, "Time dependent recovery of passive neutrophils after large deformation", *Biophys. J.*, **60**, 856-866, (1991).
- [37] G. Agresar, J.J. Linderman, G. Tryggvason and K.G. Powell, "An adaptive, Cartesian, front-tracking method for the motion, deformation and adhesion of circulating cells", *J. Comput. Phys.*, **143**, 346-380, (1998).
- [38] E. Evans and A. Yeung, "Apparent viscosity and cortical tension of blood granulocytes determined by micropipet aspiration", *Biophys. J.*, **56**(1), 151-160, (1989).
- [39] R.M. Hochmuth, "Micropipette aspiration of living cells", *J. Biomech.*, **33**, 15-22, (2000).
- [40] H-C. Kan, H.S. Udaykumar, W. Shyy and R. Tran-Son-Tay, "Hydrodynamics of a compound drop with application to leukocyte modeling", *Phys. Fluids*, **10**(4), 760-774, (1998).

-
- [41] S.V. Marella and H.S. Udaykumar, "Computational analysis of the deformability of leukocytes modeled with viscous and elastic structural components", *Physics of Fluids*, **16(2)**, 244 - 264, (2004).
- [42] W. Wang, Y. Huang, M. Grujicic, and D.B. Chrisey, "Study of Impact-Induced Mechanical Effects in Cell Direct Writing Using Smooth Particle Hydrodynamic Method", *Journal of Manufacturing Science and Engineering*, **130**, 021012-1, (2008).
- [43] G. Tryggvason, B. Bunner, A. Esmaeeli, D. Juric, N. Al-Rawahi, W. Tauber, J. Han, S. Nas and Y.J. Jan, "A front-tracking method for the computations of multiphase flow", *J. Comput. Phys.*, **169**, 708 (2001).
- [44] S.O. Unverdi and G. Tryggvason, "A front-tracking method for viscous incompressible multiphase flows", *J. Comput. Phys.*, **100**, 25 (1992).
- [45] M. Muradoglu and S. Tasoglu, "A front-tracking method for computational modeling of impact and spreading of viscous droplets on solid walls", *Computers & Fluids*, **39(4)**, 615-625 (2010).
- [46] S.F. Kistler, "Hydrodynamics of wetting", Wettability edited by Berg J.C., Marcel Dekker, *New York* (1993).
- [47] H. Takamatsu and B. Rubinsky, "Viability of Deformed Cells", *Cryobiology*, **39**, 243-251 (1999).
- [48] C. Peskin, "Numerical analysis of blood flow in the heart", *J. Comput. Phys.*, **25**, 20 (1977).
- [49] Y.H. Mori, "Configurations of gas-liquid 2-phase bubbles in immiscible liquid media", *Int. J. Multiphase Flow*, **4**, 383-396 (1978).
- [50] S. Kawano, H. Hashimoto, A. Ihara and T. Azima, "Small-amplitude oscillations of encapsulated liquid drop interfaces", *JSME International Journal Series B-Fluids and Thermal Engineering*, **40 (1)**, 33-41, (1997).

-
- [51] M. Hoorfar, M.A. Kurz, Z. Policova, M.L. Hair, A.W. Neumann, J. A. Mann, "Surface properties of sugar solutions", *80th ACS Colloid and Surface Science Symposium*, University of Colorado, Boulder, CO, (2006).
- [52] T. Chinyoka, Y.Y. Renardy, M. Renardy, D.B. Khismatullin, "Two-dimensional study of drop deformation under simple shear for Oldroyd-B liquids", *J. Non-Newtonian Fluid Mech.* 130 45–56, (2005)
- [53] R. W. Hooper, V. F. Almeida, C. W. Macoskoa, J. J. Derby, "Transient polymeric drop extension and retraction in uniaxial extensional flows", *J. Non-Newtonian Fluid Mech.* 98, 141–168, (2001)
- [54] D. Khismatullin, Y. Renardy, M. Renardy, "Development and implementation of VOF-PROST for 3D viscoelastic liquid–liquid simulations", *J. Non-Newtonian Fluid Mech.* 140, 120–131, (2006)
- [55] S. Ramaswamy, L.G. Leal, "The deformation of a Newtonian drop in the uniaxial extensional flow of a viscoelastic liquid", *J. Non-Newtonian Fluid Mech.* 88, 149-172, (1999)
- [56] P. Yue, J. J. Feng, C. Liu, J. Shen, "Transient drop deformation upon startup of shear in viscoelastic fluids", *Physics of Fluids*, 17, 123101, (2005)
- [57] E.M. Toose, B.J. Geurts, J.G.M. Kuerten, "A boundary integral method for two-dimensional (non)-Newtonian drops in slow viscous flow", *J. Non-Newtonian Fluid Mech.*, 60, 129-154, (1995)
- [58] N. Aggarwal, K. Sarkar, "Deformation and breakup of a viscoelastic drop in a Newtonian matrix under steady shear", *J. Fluid Mech.*, vol. 584, 1–21, (2007)
- [59] C. Zhou, P. Yue, J. Feng, "Simulation of Neutrophil Deformation and Transport in Capillaries using Newtonian and Viscoelastic Drop Models", *Annals of Biomedical Engineering*, Vol. 35, 766–780, (2007)

- [60] E.M. Toose, B.J. Geurts and J.G.M. Kuerten, "A 2D boundary element method for simulating the deformation of axisymmetric compound non-Newtonian drops", *International Journal for Numerical Methods in Fluids*, Vol. 30, 653-674, (1999)
- [61] J. C. Tannehill, D. A. Anderson, R. H. Fletcher, "Computational fluid mechanics and heat transfer", Taylor & Francis, Philadelphia, (1997)

VITA

GÖZDE KAYNAK was born in Istanbul, Turkey on August 20, 1986. She received her B.Sc. degree in Mathematical Engineering from Istanbul Technical University in 2008. She worked as a teaching and research assistant with full scholarship in Koc University, Istanbul.